Journal of Catalysis 459 (2026) 116924

Contents lists available at ScienceDirect

Journal of Catalysis

journal homepage: www.elsevier.com/locate/jcat

Liquid-phase direct oxidation of methane to methanol: systematic study of copper speciation, dispersion, zeolite acidity, and framework aluminum coordination

Luis A. Gallego-Villada [a,*], Päivi Mäki-Arvela [a], Kari Eränen [a], Pasi Virtanen [a], Narendra Kumar [a], Mika Lastusaari [b], Dmitry Yu. Murzin [a,*]

[a] Laboratory of Industrial Chemistry and Reaction Engineering, Johan Gadolin Process Chemistry Centre, Åbo Akademi University, Henriksgatan 2, 20500 Turku/Åbo, Finland

[b] University of Turku, Department of Chemistry, FI-20014 Turku, Finland

ARTICLE INFO

Keywords:
Methane
Methanol
Cu-ZSM-5
Copper dispersion
BAS-LAS pair
Isolated Cu^{2+} species

ABSTRACT

The direct oxidation of methane to methanol (DOMTM) remains challenging due to the low reactivity of methane and difficulties in achieving high activity and selectivity under mild conditions. In this work, Cu-ZSM-5 catalysts were systematically investigated using H_2O_2 as oxidant in water at 50 °C to establish quantitative structure–activity relationships. Comprehensive characterization of copper speciation, dispersion, acidity, and framework aluminum coordination was performed. Preservation of the MFI structure was confirmed by X-ray diffraction, while Brønsted and Lewis acid sites were quantified using pyridine adsorption, and framework and extra-framework aluminum coordination was determined by ^{27}Al solid-state NMR. Copper dispersion, quantified by N_2O oxidation–H_2 reduction (TPR), along with UV–Vis diffuse reflectance spectroscopy and H_2-TPR, indicated the presence of isolated Cu^{2+} species. Turnover frequency exhibited non-monotonic dependencies on Brønsted acid site density and BAS/LAS ratio. Methanol formation was maximized (productivity of 750 μmol g^{-1} h^{-1} with a selectivity of 49% to methanol) within Brønsted acid site densities of 0.58–0.96 μmol m^{-2} and BAS/LAS ratios of 1.0–1.7, highlighting the synergistic effect of BAS-LAS pairs. These results demonstrate that high methanol productivity arises from a cooperative interplay between copper dispersion, acid site density, and BAS-LAS synergy. Rigorous quantification of all oxidation products (CH_3OOH, CH_3OH, HCHO, HCOOH, CO_2) enabled accurate evaluation of catalytic performance under low-conversion conditions.

1. Introduction

Methane (CH_4) is an abundant and relatively clean fossil energy source, present in natural gas with compositions reaching up to 80–90%, and in shale gas, where it is typically found together with ethane as a major component [1,2]. Compared with many other hydrocarbons, methane provides the highest heat of combustion (55.5 MJ kg^{-1}). Consequently, it has been widely utilized in industry and daily human activities, supplying a significant fraction of the current global energy demand [2]. However, the storage and transportation of natural gas remain major obstacles to its utilization due to an inherently low volumetric energy density [3]. For this reason, extracted natural gas is usually stored and transported as liquefied natural gas (LNG), which requires cooling below its boiling point (≈ −162 °C). This approach, however, has several major drawbacks, including high infrastructure costs and significant methane leakage, which is a potent greenhouse gas with a global warming potential (GWP) estimated to be 28–36 times higher than that of CO_2 over a 100-year time horizon [2–4]. Given these limitations, converting methane into liquid products represents a more convenient and potentially economical alternative for storage and transportation.

Traditional industrial processes convert methane first into synthesis gas (a CO/H_2 mixture), which is subsequently transformed into liquid hydrocarbons via the Fischer-Tropsch process. These routes are energy-intensive and involve multiple reaction steps [2,3]. Methane can also be directly pyrolyzed to olefins or aromatic hydrocarbons, or coupled to C_2 products at very high temperatures [5]. Among all direct conversion routes, the selective direct oxidation of methane to methanol (DOMTM,

* Corresponding authors.
E-mail addresses: luis.gallegovillada@abo.fi (L.A. Gallego-Villada), dmitry.murzin@abo.fi (D.Yu. Murzin).

https://doi.org/10.1016/j.jcat.2026.116924
Received 20 February 2026; Received in revised form 2 April 2026; Accepted 22 April 2026
Available online 29 April 2026

Fig. 1a) remains a long-standing challenge in catalysis due to the high C–H bond strength of methane (439 kJ mol^{-1}) and its chemical inertness [6–8]. Nevertheless, continued investigation is justified, as this reaction is thermodynamically favorable under relatively mild conditions (Fig. 1b) and avoids energy-intensive intermediate steps [2].

Global methanol demand reached approximately 120 million tonnes in 2024 [9], with more than 60% consumed as a chemical feedstock for the production of olefins, formaldehyde, and acetic acid [4]. Methanol also contributes to the transportation fuel sector, both as a chemical intermediate, primarily for methyl *tert*-butyl ether production (~11%) and biodiesel synthesis (~3%), and additionally as a direct fuel or gasoline blend (~11%) [4].

Significant effort has been devoted in the recent years to the DOMTM route, resulting in the exploration of a wide range of heterogeneous catalytic systems. Table S1 summarizes representative examples, grouped into broad catalyst families to enable a meaningful comparison of the strategies that have been pursued. Early studies focused on homogeneous-heterogenized metallophthalocyanine complexes supported on zeolitic or siliceous matrices (CuPc, FePc, and CoPc on X, Y, and L zeolites; entries 1–6, Table S1). These systems represent attempts to mimic enzymatic active sites; however, they display negligible or very poor methanol formation, highlighting their inability to control the formation and reactivity of radical intermediates, such as hydroxyl and methyl radicals [4], under liquid-phase reaction conditions [9]. The immobilization of molecular iron complexes, exemplified by $(FePc^{t}Bu_4)_2N@SiO_2$ (entry 7, Table S1) [10], modestly improved stability but did not fundamentally overcome the limitations in activity or selectivity.

Later work was shifted toward isolated or clustered Fe- and Cu-based sites in microporous materials (entries 8–9, 16, 18–19, Table S1), such as Fe/silicalite-1 and Cu/silicalite-1 [11], Ag_1-Cu_1/ZSM-5 [12], 1Cu/2Zn-ZSM-5 [13], and Cu-ZSM-5 [14], as well as Cu-based species in mesoporous silicas (entries 10–11, Table S1), such as CuEtp@AlMSN30-ex [15] and CuEtp@MSN-TP [15]. As clearly illustrated in Fig. 1c, these catalysts achieve high methanol selectivities and, in some cases, high productivities. However, this performance is significantly associated with the use of H_2O_2 (either as a commercial reagent or generated in situ) rather than molecular oxygen. Consequently, the impressive productivity reported for these materials reflects peroxide-driven chemistry rather than a genuine progress toward selective O_2-based methane oxidation.

A third family comprises noble-metal catalysts (Au [16,17], Pd [16], Au-Pd [16,18], Rh [19]) supported on carbon nanotubes or acidic zeolites and operates with molecular oxygen or O_2/H_2 mixtures (entries 12–15, 20–21, Table S1). These materials are closer to the desired objective of using O_2 directly; nevertheless, as Fig. 1c makes evident, they typically suffer from low methane conversion and only moderate methanol productivities, even when selectivity is acceptable. Therefore, the limitation here is not selectivity per se, but insufficient activation of methane under mild conditions. More recently, structurally well-defined iron-containing materials, such as the metal–organic framework DUT-5-$Fe(OH)_2$ (entry 17, Table S1) [20], have been proposed as an alternative strategy, showing good selectivity but still requiring either elevated

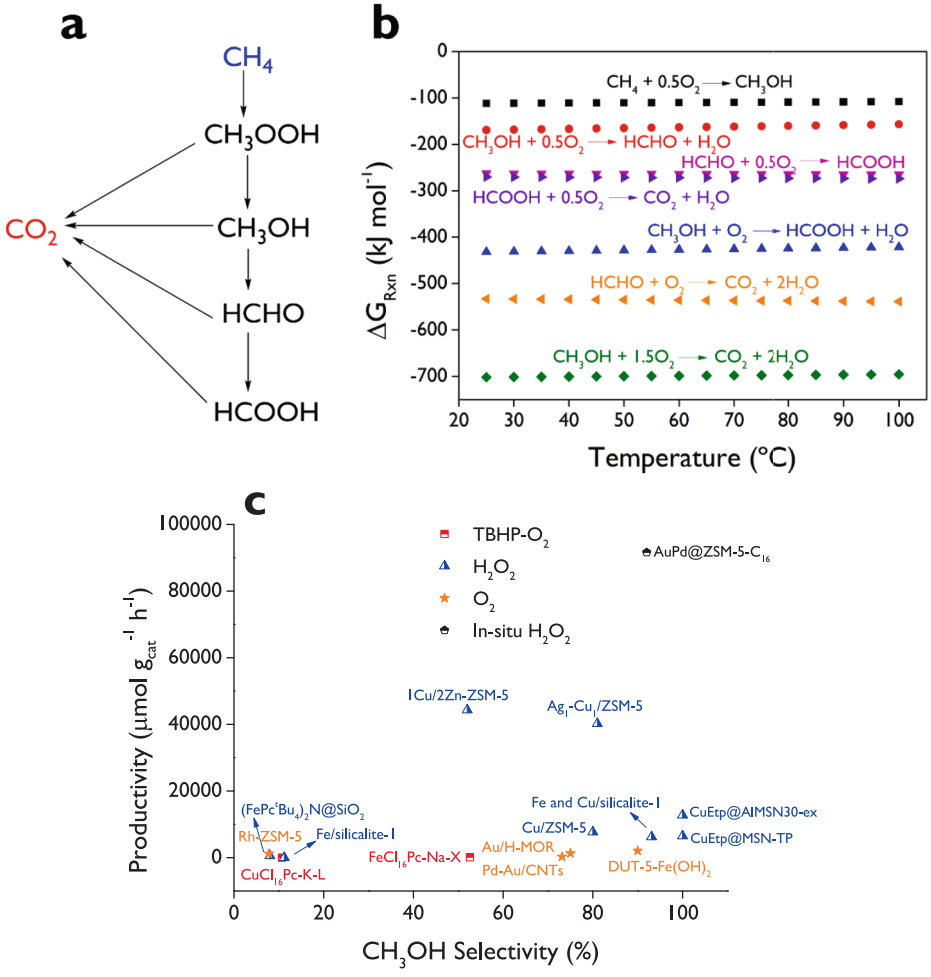

Fig. 1. (a) Reaction network of a typical DOMTM route. **(b)** Gibbs free energy changes for various reactions participating in CH_4 oxidation. **(c)** Methanol productivity for different oxidants.

temperatures (125 °C) or very long reaction times (up to 40 h).

Overall, it is observed through the comparison across catalysts that high methanol selectivity and high productivity are rarely achieved simultaneously, and, in those cases, this performance is achieved using H_2O_2 as the oxidant rather than molecular oxygen. Consequently, the simultaneous achievement of high activity, high selectivity, and the direct utilization of molecular oxygen remains an unresolved challenge in methane-to-methanol catalysis.

As shown in Fig. 1c, Cu-ZSM-5 was selected in this work as a representative model catalyst to systematically investigate the direct oxidation of methane to methanol. The MFI framework allows controlled variation of copper speciation, dispersion, acidity, and aluminum environment under relatively mild reaction conditions. The catalytic performance of Cu-ZSM-5 is known to depend on the nature, loading, dispersion, and reducibility of copper species, the method of metal incorporation, the density and balance of Brønsted and Lewis acid sites, and the spatial distribution and coordination of framework aluminum. However, these dependencies have typically been established through isolated or independent studies focusing on individual effects rather than through a comprehensive evaluation of all relevant parameters. Although numerous studies have addressed metal-modified ZSM-5 catalysts for liquid-phase methane oxidation [4,12,13,16], a systematic assessment integrating these interdependent factors remains lacking. Moreover, some reports in the literature provide incomplete quantification of oxidation products, particularly dissolved CO_2 [21], which is frequently overlooked, limiting accurate assessment of product distribution.

This work aims to establish robust structure–activity relationships for DOMTM over Cu-ZSM-5 using a comprehensive experimental approach. Specifically, methane oxidation is carried out using H_2O_2 as the oxidant, water as the solvent, and Cu-ZSM-5 as the catalyst, using different methods of Cu incorporation. An integrated characterization strategy is applied, encompassing crystallinity and phase purity (XRD), morphology and elemental distribution (SEM-EDX, TEM), textural properties (N_2 physisorption), acid site density (pyridine-FTIR), copper loading (EDX) and dispersion (TEM, N_2O oxidation, H_2-TPR), reducibility (H_2-TPR), copper speciation (UV–Vis-DRS and H_2-TPR), and the coordination and spatial distribution of framework aluminum (^{27}Al and ^{29}Si MAS NMR). Importantly, in this work, all products along the methane oxidation pathway (Fig. 1a), such as methyl hydroperoxide, methanol, and typical over-oxidation products (formaldehyde, formic acid, and CO_2), are rigorously quantified using HPLC, ^{1}H NMR, and potentiometric titration, with methane conversions reported even at very low levels. This comprehensive methodology provides new insights into the fundamental structure–activity relationships governing DOMTM over Cu-ZSM-5 and establishes a benchmark for future studies, addressing the frequent omission in mentioning that conversion is very low (often <1%) and not reporting in the literature data for by-products.

2. Materials and methods

2.1. Reagents

Commercial zeolites supplied by Zeolyst International were used as starting materials for catalyst synthesis. The selected zeolites possessed the MFI structure and were provided in the ammonium form: CBV 2314 (SiO_2/Al_2O_3 molar ratio = 23), CBV 3024E (SiO_2/Al_2O_3 molar ratio = 30), CBV 5524G (SiO_2/Al_2O_3 molar ratio = 50), and CBV 8014 (SiO_2/Al_2O_3 molar ratio = 80). Copper(II) nitrate trihydrate ($Cu(NO_3)_2{\cdot}3H_2O$, 98.0 wt%, Alfa Aesar) was used as the copper precursor. Methane (CH_4, 99.995%, Woikoski) and hydrogen peroxide solution (H_2O_2, 30 wt%, Sigma-Aldrich) were used as materials for the catalytic tests. For quantification using HPLC, formaldehyde solution (HCHO, 36 wt%, stabilized with ~10 wt% methanol, VWR Chemicals), formic acid (HCOOH, ≥ 98 wt%, Sigma-Aldrich), and methanol (CH_3OH, HPLC grade, ≥ 99.9 wt%, Sigma-Aldrich) were employed as standards. For quantification by NMR, deuterium oxide (D_2O, 99.8 atom% D, Thermo Scientific) and 3-trimethylsilyl-1-propanesulfonic acid sodium salt (DSS, $(CH_3)_3Si(CH_2)_3SO_3Na$, European Pharmacopoeia Reference Standard) were used. Sodium hydroxide solution (0.1 mol L^{-1} NaOH, carbonate-free, Fischer Chemical) was used to prepare the titrant agent (0.01 mol L^{-1}) in potentiometric titration. Other chemicals used during the experimental work were: sulfuric acid (H_2SO_4, 96%, Merck), helium (He, 99.996%, Linde), nitrous oxide (N_2O, 0.5 mol% in He, Linde), argon (Ar, 99.999%, Linde), and hydrogen (H_2, 5.24% in Ar, Woikoski).

2.2. Catalyst preparation

The H^+ form of the zeolites was obtained via calcination of the NH_4^+ form in static air, using a two-step process. Initially, the temperature increased from room temperature to 350°C at a rate of 1.8 °C min^{-1} and held for 4 h. Subsequently, the temperature was raised to 550 °C at 1.7 °C min^{-1} and maintained for 4 h. These materials were designated as ZSM-5-X, where X denotes the nominal SiO_2/Al_2O_3 molar ratio (X = 23, 30, 50, or 80).

Copper-modified ZSM-5 catalysts were synthesized using three distinct methods to prepare materials with a wide range of Cu loading: ion exchange (IE), wetness impregnation (WI), and evaporation impregnation method (EIM). For the ion exchange method (IE), a 0.02 mol L^{-1} aqueous solution of copper(II) nitrate trihydrate was prepared. The precursor solution (100 mL per gram of zeolite) was added to the NH_4^+-form zeolite (5 g in a typical experiment). The resulting suspension was transferred to a 1000 mL flask, heated to 60 °C, and stirred at 300 rpm for 24 h using a Rotavapor (Buchi Instrument R-114). After the synthesis was completed, the solid was recovered by filtration, washed with distilled water, and dried at 105 °C in static air overnight.

For the evaporation impregnation method (EIM), a copper loading of 5 wt% was targeted. The appropriate amount of copper salt was dissolved in distilled water (20 mL per g of zeolite), and the solution was added to the NH_4^+-form zeolite (5 g in a typical experiment) in a 250 mL flask. The mixture was stirred at 300 rpm for 1 h at room temperature. The resulting solid was obtained by evaporating water, followed by drying at 105 °C.

For the wetness impregnation method (WI), the same amount of copper precursor was used as in the EIM method, under otherwise identical conditions. However, in this case, the solid was recovered by filtration and subsequently dried at 105 °C. Due to the filtration involved in this method, lower copper loading than the nominal 5 wt% is expected, typically resulting in intermediate copper contents between those obtained by IE and EIM.

All Cu-based catalysts were calcined using the same two-step treatment described above for the H^+-form zeolites. The final catalysts were denoted as Cu-ZSM-5-X-M, where X corresponds to the nominal SiO_2/Al_2O_3 molar ratio (X = 23, 30, 50, or 80), and M indicates the copper incorporation method (M = IE, EIM, or WI).

2.3. Catalyst characterization

The prepared catalysts were extensively characterized to investigate the crystalline structure by X-ray diffraction (XRD), textural properties (N_2 physisorption), acidity (pyridine-FTIR), and framework composition (^{27}Al and ^{29}Si MAS NMR). The nature of copper species was examined by UV–Vis diffuse reflectance spectroscopy (DRS) and H_2-TPR, while morphology and particle size were evaluated by TEM and SEM. Copper dispersion was estimated from TEM analysis and independently determined by the N_2O selective oxidation combined with temperature-programmed reduction (s-TPR), complemented by conventional H_2-TPR measurements. Copper leaching was investigated by ICP-OES and XRF. Full experimental procedures, instrumental conditions, and calculation details are provided in Section 2 of the Supporting Information.

2.4. Catalytic tests

The catalytic performance tests were carried out in a 300 mL high-pressure batch autoclave reactor (Parr Instrument Co., model TS-10/350C, part No. 452HCTC; material: T316 stainless steel; maximum working pressure: 200 bar; serial No. 25043). To avoid undesired decomposition of hydrogen peroxide upon a contact with metal surfaces, a Teflon liner was used inside the autoclave. The effective reaction volume was estimated to be 218 mL, accounting for the Teflon liner volume (62 mL) and approximately 20 mL corresponding to the stirrer shaft and internal tubing.

The reactor was equipped with a mechanical stirrer (IKA Eurostar), an internal thermocouple, a cooled sampling valve, and an auxiliary cooling line to control the internal temperature of the system. The cooling system was connected to the sampling valve, maintaining the temperature below 10 °C during sampling to minimize volatilization losses of oxygenated products. The reaction was initiated by charging the Teflon liner with 70 mL of deionized water containing 0.5 mol L^{-1} H_2O_2 as the oxidant. Then, 150 mg of the catalyst was added to the solution. The autoclave was then properly assembled and sealed. Thereafter, the reactor was purged four times with N_2, followed by four additional purges with CH_4. After the purging steps, the system was pressurized with methane to an initial pressure of 30 bar at room temperature. Subsequently, the reactor was heated to the reaction temperature of 50 °C under the lowest speed of the stirrer (approx. 50 rpm). Once the setpoint temperature was reached, the stirring speed was immediately increased to 1000 rpm, marking the start time of the reaction. As the temperature stabilized, the internal pressure increased, reaching a final pressure of approximately 32.5 – 33 bar. Additionally, when the samples were collected at specific time intervals, they were filtered using 13 mm, 0.45 µm PVDF syringe filters to ensure the removal of catalyst particles prior to analysis by HPLC, NMR, and potentiometric titration. Catalytic tests were performed using a high stirring speed (1000 rpm) and small catalyst particles (<150 µm) to suppress external and internal mass transfer limitations, respectively.

2.5. Quantification of products

Liquid-phase products were quantified by HPLC using a Rezex™ ROA-Organic Acid H^+ (8%) column on an Agilent 1100/1200 system with 0.005 mol L^{-1} H_2SO_4 as the mobile phase and refractive index detection. Product identification was further confirmed by ^1H NMR spectroscopy (Bruker 600 MHz) using D_2O with DSS as an internal standard and solvent suppression to minimize water interference. Dissolved CO_2 in the aqueous phase was determined by potentiometric titration with standardized NaOH, subtracting the contribution of formic acid independently quantified by HPLC. Detailed experimental conditions, calibration data, representative chromatograms and spectra, and titration procedures are provided in Section 3 of the Supporting Information (Table S2, Figs. S1-S4).

Gas-phase products were analyzed during preliminary experiments by gas chromatography (HP 6890 series, TCD) using syringe samples collected from the reactor outlet after 4 h of reaction. CO was not detected, while CO_2 was quantified in minor amounts (<2% of total carbon products, Fig. S5). Therefore, gas-phase analysis was not included in the routine quantification protocol. Liquid-phase samples were collected through a cooled sampling valve to near-ambient conditions before analysis, as stated in section 2.4. Under these conditions, and given the relatively high solubility of CO_2 in water, most of the CO_2 remains dissolved in the liquid phase. CO_2 was therefore quantified by potentiometric titration of the liquid phase.

The methane conversion to oxygenated products (X_{OP}) and the selectivity to the oxygenated product (S_i) were calculated from the HPLC results according to Eqs. (1)–(2), where the detected oxygenated were methyl hydroperoxide (CH_3OOH), methanol (CH_3OH), and formic acid (HCOOH). The number of moles of compound i (n_i) was determined using multipoint calibration curves based on external standards (Fig. S1).

$$X_{OP}(\%) = \frac{\text{mol oxygenated products}}{\text{Initial mol } CH_4} \times 100 = \frac{n_{CH_3OOH} + n_{CH_3OH} + n_{HCOOH}}{n_{CH_4,0}} x100 \quad (1)$$

$$S_i(\%) = \frac{n_i}{n_{CH_3OOH} + n_{CH_3OH} + n_{HCOOH}} \times 100 \quad (2)$$

The conversion of hydrogen peroxide ($X_{H_2O_2}$) as the oxidizing agent was calculated using Eq. (3), where $n_{H_2O_2,0}$ and $n_{H_2O_2,t}$ correspond to the initial and final (at time t) moles of H_2O_2, respectively·H_2O_2 was also monitored and quantified by HPLC.

$$X_{H_2O_2}(\%) = \frac{n_{H_2O_2,0} - n_{H_2O_2,t}}{n_{H_2O_2,0}} \times 100 \quad (3)$$

Methanol productivity was calculated based on both the catalyst mass (m_{cat}) and the copper mass (m_{Cu}), according to Eqs. (4) and (5), respectively. The copper mass was calculated using the Cu loading (wt. %) determined by SEM-EDX.

$$Prod_{CH_3OH}(\mu mol\, g_{cat}^{-1}) = \frac{n_{CH_3OH}}{m_{cat}} \quad (4)$$

$$Prod_{CH_3OH}(\mu mol\, mg_{Cu}^{-1}) = \frac{n_{CH_3OH}}{m_{Cu}} = \frac{n_{CH_3OH}}{m_{cat}\, x\, Cu(wt.\%)} \quad (5)$$

The total methane conversion (X_T) and the selectivity to all products ($S_{i,L}$) in the liquid phase (oxygenated compounds and CO_2) were calculated using Eqs. (6) and (7), at a final reaction time of 4 h, unless otherwise specified. The results were obtained using potentiometric titration for the quantification of CO_2 dissolved in the liquid phase, and NMR analysis, which allowed the quantification of formaldehyde (in the form of methanediol), since HPLC is not sensitive enough to detect formaldehyde at the concentrations used in this study.

$$X_T(\%) = \frac{(n_{CH_3OOH} + n_{CH_3OH} + n_{HCOOH})_{HPLC} + (n_{HCHO})_{NMR} + n_{CO_2}}{n_{CH_4,0}} \times 100 \quad (6)$$

$$S_{i,\,L}(\%) = \frac{n_i}{n_{CH_4,0}\, x\, X_T} \times 100 \quad (7)$$

The turnover frequency (TOF) for methanol in the direct oxidation of methane to methanol (DOMTM) was calculated based on the total acidity (TOF_A) and the Cu dispersion (TOF_D), according to Eqs. (8) and (9), respectively, where $n_{CH_3OH,\,\Delta t}$ correspond to the produced moles of methanol after a time interval of $\Delta t = 15$ min, m_{cat} is the catalyst mass, TA is the total acidity referred to the sum of Brønsted and Lewis acidity of the catalyst, n_{Cu} is the moles of Cu, and D_{Cu,N_2O} is the surface copper dispersion calculated by the N_2O oxidation method.

$$TOF_A = \frac{n_{CH_3OH,\,\Delta t}}{m_{cat}\, x\, TA\, x\, \Delta t} \quad (8)$$

$$TOF_D = \frac{n_{CH_3OH,\,\Delta t}}{n_{Cu}\, x\, D_{Cu,N_2O}\, x\, \Delta t} \quad (9)$$

3. Results and discussion

3.1. Structural and morphological properties

The XRD patterns of the prepared catalysts are shown in Fig. 2. All samples exhibit the characteristic reflections of the MFI framework (PDF code: 04-008-8144), with peaks at 7.9°, 9.1°, 23.1°, 23.3°, 23.9°, and 24.4°, assigned to the (101), (111), (332), (051), (303), and (133) planes, respectively [22]. Although the formation of CuO might be expected after calcination, no distinct Cu-oxide reflections are observed. This absence is likely due to the low Cu loading (EDX, Table 1) and/or

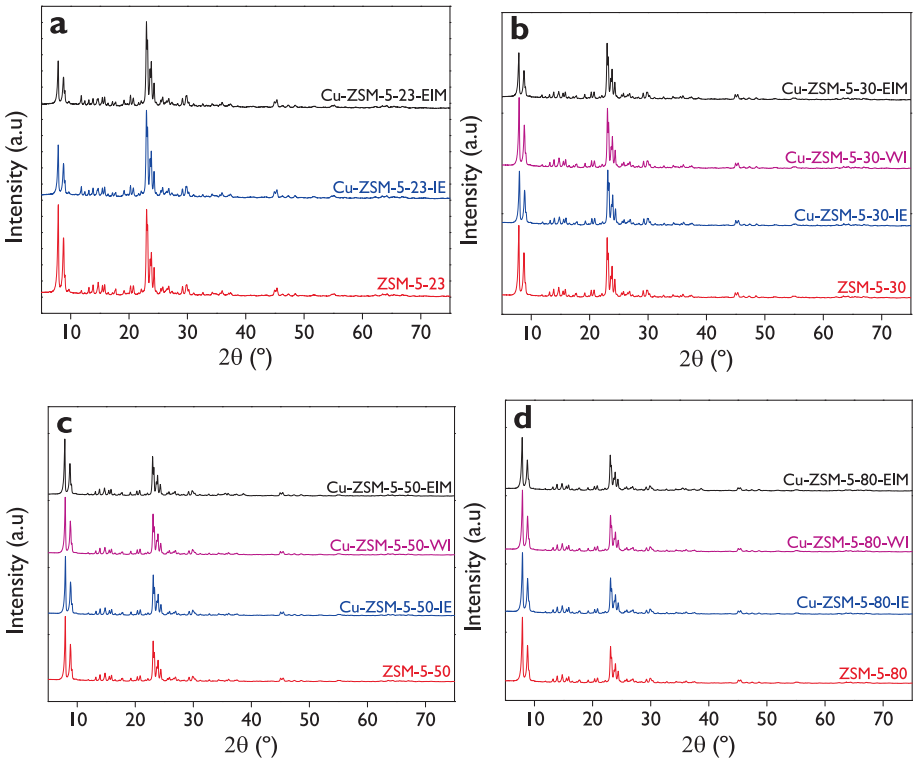

Fig. 2. XRD patterns of catalysts based on **(a)** ZSM-5-23, **(b)** ZSM-5-30, **(c)** ZSM-5-50, and **(d)** ZSM-5-80.

the presence of highly dispersed Cu species with domains too small or too disordered to generate detectable diffraction peaks [23]. Previous reports indicate that CuO reflections in zeolite-supported systems are observable at higher Cu loadings (≈ 10–12 wt%) on zeolite Y, showing peaks at 35.5° and 38.9°, assigned to the (200) and (002) planes [24]. These peaks are not visible in Fig. 2 because the maximum Cu content is only 4.1 wt% for Cu-ZSM-5-23-EIM (Table 1). On the other hand, the XRD patterns of the spent materials (Fig. S6) indicate that the zeolitic framework remained intact during the DOMTM reaction, as evidenced by the unchanged diffraction features of the fresh and spent samples. Although ICP-OES analysis showed a decrease in Cu content from 0.61 wt% to 0.18 wt% between fresh and spent Cu-ZSM-5-30-WI (Table S3), this reduction cannot be attributed exclusively to Cu leaching, as the spent solid was dried at room temperature and was not treated before analysis. Therefore, it retained adsorbed water and reaction products that dilute the measured Cu weight fraction. XRF analysis of the post-reaction liquid phase confirmed that the Cu concentration in the solution was minimal (<1% of total dissolved species, Table S4), indicating that Cu leaching under the studied reaction conditions is limited, although not entirely negligible. Notably, Si was identified as the major dissolved species among the detectable species (52.6 ± 2.4%, Table S4), suggesting partial dissolution of the ZSM-5 framework under the mildly acidic conditions generated during the reaction by formic acid.

SEM micrographs of the fresh catalysts (Fig. S7) provide information on the crystal size and crystalline morphology, generally revealing well-defined, anisotropic ZSM-5 crystals with a coffin-shaped morphology, consistent with crystal growth characteristics of the MFI framework. In addition to the dominant morphology, the samples exhibit morphological heterogeneity, including smaller rounded crystallites and plate-like crystallites arranged in stacked or intergrown domains, leading in some cases to pseudo-cubic aggregate-like features. The characteristic crystal dimensions observed by SEM are typically in the range of 100–200 nm, in agreement with previously reported values [25]. Overall, these observations confirm the well-defined crystalline morphology of the synthesized catalysts. The SiO_2/Al_2O_3 molar ratios calculated from the EDX data (Table S5) are in good agreement with the nominal values provided by the supplier for the parent ZSM-5 supports (23, 30, 50, and 80). Although EDX is inherently surface-sensitive and therefore not expected to reproduce bulk compositions with exact numerical accuracy, the measured ratios follow the correct trend and remain close to the nominal values across all samples.

3.2. Textural properties and Cu content

The N_2 adsorption–desorption isotherms of the catalysts are shown in Fig. 3, while Table 1 presents an overview of the textural properties for all the catalysts. All the materials exhibited hybrid type I(a) and IV(a) isotherms due to the presence of both micropores and mesopores, even in the pristine zeolites, demonstrating that the mesoporosity associated with the samples can be attributed to intrinsic features of the commercial material, as has been previously reported for MFI framework (H-CVB-80) [26], but also for other zeolitic frameworks like faujasite [27] and beta [28]. All the prepared materials exhibit a strong N_2 adsorption at very low relative pressures ($P/P_o < 0.001$), typical of filling the micropores [29]. A small hysteresis at intermediate relative pressures ($P/P_o \sim 0.4 – 0.9$) is observed in all samples, indicative of mesoporosity, although it is more pronounced for the high-silicon samples (Fig. 3c–d), which exhibited a lower fraction of microporosity than the catalysts supported on ZSM-5–23 and ZSM-5–30 (Table 1). Differences among Cu incorporation methods are also evident: EIM samples show slightly reduced adsorption (low surface areas, Table 1) due to partial blocking of micropores by Cu species, whereas WI and IE maintain higher accessibility.

The specific surface area was initially estimated using the Dubinin-Radushkevich (DR) method (Table S6), which is typically applied to microporous solids [23]. However, because the statistical thermodynamic fluctuation theory (STFT) is considered a more robust approach, free from the assumptions and limitations of the BET method, it was adopted as the primary method in this work [30]. Accordingly, the values reported in Table 1 were obtained using STFT. The deviation between the STFT and DR results ranged from 0% to 3%, whereas the differences relative to the BET areas (Table S6) were substantially larger, with deviations ranging from 2% to 35% across the samples.

Table 1
Textural properties of the prepared catalysts. Values for the spent catalysts are shown in parentheses.

Catalyst	Cu[a] (wt.%)	SA (m^2/g)	dSA[b] (%)	V_{Mic} ($cm^3\ g^{-1}$)	V_T ($cm^3\ g^{-1}$)	Microporosity[c] (%)
ZSM-5-23	0.0	446	n.d	0.217	0.223	97.1
Cu-ZSM-5-23-IE	2.4	431 (413)	−4	0.210 (0.193)	0.218 (0.193)	96.1 (100.0)
Cu-ZSM-5-23-EIM	4.1	419 (413)	−1	0.186 (0.189)	0.186 (0.191)	100.0 (99.0)
ZSM-5-30	0.0	430 (472)	10	0.211 (0.228)	0.234 (0.242)	90.4 (94.1)
Cu-ZSM-5-30-IE	0.6	487 (438)	−10	0.239 (0.218)	0.255 (0.239)	93.5 (91.3)
Cu-ZSM-5-30-EIM	3.6	394 (400)	2	0.182 (0.193)	0.182 (0.199)	100.0 (97.2)
Cu-ZSM-5-30-WI	0.4	426 (443)	4	0.210 (0.215)	0.228 (0.234)	92.3 (91.8)
ZSM-5-50	0.0	458	n.d	0.225	0.250	90.1
Cu-ZSM-5-50-IE	0.9	432 (471)	9	0.207 (0.235)	0.227 (0.259)	91.3 (90.7)
Cu-ZSM-5-50-EIM	3.2	417	n.d	0.198	0.198	100.0
Cu-ZSM-5-50-WI	0.6	452 (451)	−0.3	0.222 (0.225)	0.244 (0.242)	91.0 (93.1)
ZSM-5-80	0.0	480	n.d	0.236	0.271	87.0
Cu-ZSM-5-80-IE	0.7	523	n.d	0.254	0.292	86.8
Cu-ZSM-5-80-EIM	3.2	439 (422)	−4	0.211 (0.210)	0.253 (0.233)	83.2 (89.9)
Cu-ZSM-5-80-WI	0.5	461 (459)	−0.4	0.225 (0.228)	0.260 (0.263)	86.4 (86.6)

SA: Surface area, $\mathbf{V_{Mic}}$**:** Micropores volume, $\mathbf{V_T}$**:** Total pore volume.
[a] The weight percentage of Cu was determined by SEM-EDX (Table S5).
[b] $dSA = (SA_{Spent} - SA_{Fresh})/SA_{Fresh}$.
[c] Microporosity = V_{Mic}/V_T. n.d: not determined. **Reaction conditions for the spent catalysts:** 30 bar CH_4 at room temperature, 0.5 mol L^{-1} H_2O_2 in deionized water, 70 mL total volume, 150 mg catalyst, 50 °C, 1000 rpm.

The introduction of Cu into the ZSM-5 framework produced structural effects that varied significantly with both the Si/Al ratio and the incorporation method. The Cu contents determined by SEM-EDX are reported in Table 1. In general, the samples with the highest Cu loadings (4.1%, 3.6%, and 3.2%), prepared via the EIM route, exhibited the most systematic changes, characterized by clear reductions in surface area and micropore volume, with microporosity values reaching 100%, except for Cu-ZSM-5-80-EIM (83.2%). These observations indicate occupation or blockage of the microporous network by copper species. Catalysts prepared by WI showed a similar decreasing trend relative to their corresponding parent zeolites, although the textural losses were consistently smaller, in line with their lower Cu loadings (0.4%, 0.6%, and 0.5%).

In contrast, the IE samples with the lowest Cu loadings (0.6% and 0.7% for Cu-ZSM-5-30-IE and Cu-ZSM-5-80-IE, respectively) did not follow the expected correlation between Cu content and porosity modification, instead exhibiting increases in the surface area relative to the parent zeolites. This behavior suggests that secondary processes inherent to the ion-exchange step, rather than copper incorporation itself, dominated the textural response. Possible contributions include the removal of occluded species or loosely bound impurities from zeolitic pores during ion exchange, which can enhance accessible surface area by unblocking channels and exchanging cations with framework sites [31], as well as slight dealumination of framework Al during aqueous ion-exchange that alters acidity and textural parameters without full structural collapse [32]. In general, the microporosity of all catalysts remained high (>83%), although it tended to decrease slightly as the SiO_2/Al_2O_3 molar ratio increased. On the other hand, the average pore size for all the fresh catalysts, in the microporosity region, was around 0.6 nm (Fig. S8).

The N_2 adsorption–desorption isotherms and pore size distributions of the spent catalysts (Fig. S9) show that the largest decrease in surface area was observed for Cu-ZSM-5–30-IE (−10%), followed by Cu-ZSM-5-23-IE and Cu-ZSM-5-80-EIM, both with dSA = -4%, which is consistent with partial pore blockage by adsorbed species, as also reflected by the reduction in total pore volume (Table 1). In contrast, some catalysts exhibited a slight increase in the surface area after the reaction, likely due to the interactions with H_2O_2, which can remove surface residues or unblock micropores, in agreement with Kurniawan et al. [33] for zeolite 13X. For certain samples, the observed variations fall within the experimental error (approximately $|dSA| \leq 3\%$). These textural changes are further consistent with the partial Si dissolution evidenced by XRF analysis of the post-reaction liquid phase (Table S4). However, the structure of the catalysts remained stable based on XRD (Fig. S6).

3.3. Aluminum coordination and accessible acidity

Although many studies are using catalytic systems for the direct oxidation of methane to methanol, employing zeolite-based materials [13,14,21], the acidity is most often treated as an implicit property rather than a systematically investigated parameter. In many cases, the presence of Brønsted or Lewis acid sites is inferred from framework composition or ion-exchange degree, without a consistent quantification or comparative analysis across catalyst series.

Only a limited number of reports have explicitly examined the role of specific acid site types. For example, in Cu-exchanged mordenite, the influence of Brønsted acid sites has been investigated, revealing a maximum methanol productivity of 118 μmol g^{-1} for samples exhibiting the highest Brønsted acidity [34]. In this work, the surface acidity of the investigated catalysts based on Cu-ZSM-5, as one of the most promising catalysts for the DOMTM reaction, is systematically analyzed.

Pyridine-FTIR was used to quantify Brønsted and Lewis acidic sites from spectra of desorbed pyridine at increasing temperatures, as presented in Fig. 4a for the Cu-ZSM-5-30-WI catalyst. As the desorption temperature increases, the intensity of both bands (Py-B and Py-L) decreases, reflecting the strength distribution of the acid sites, with weaker sites desorbing at lower temperatures and stronger sites persisting at higher temperatures. Similar trends were observed for all catalysts. The parent ZSM-5 materials are dominated by Brønsted acidity (Fig. 4b, Table S7), with values of 483, 292, 179, and 144 μmol g^{-1} representing 91.1%, 84.6%, 68.6%, and 66.4% of total acidity for ZSM-5-23, ZSM-5-30, ZSM-5-50, and ZSM-5-80, respectively, and high BAS/LAS ratios (Fig. 4b) ranging in a decreasing trend from 10.3 (ZSM-5-23) to 2.0 (ZSM-5-80). The incorporation of Cu leads to a marked increase in Lewis acidity, accompanied by a concomitant decrease in Brønsted acidity, drastically reducing the BAS/LAS ratio. For instance, in ZSM-5-23, Lewis acidity increases from 47 to 428–446 μmol g^{-1} after Cu incorporation, while the BAS/LAS ratio drops from 10.3 to 1.0 (Cu-ZSM-5-23-IE) and 0.5 (Cu-ZSM-5-23-EIM). Similar trends are observed in ZSM-5-30, where the total acidity increases from 345 μmol g^{-1} to 520 μmol g^{-1} after ion exchange (Cu-ZSM-5–30-IE), accompanied by a decrease in BAS/LAS from 5.5 to 1.2. Overall, the Cu-ZSM-5 catalysts exhibit total acidities in the range of 217 (ZSM-5-80) to 841 μmol g^{-1} (Cu-ZSM-5-23-IE), dominated by Lewis contributions, consistent with the formation of coordinately unsaturated Cu centers and partial neutralization of protonated sites.

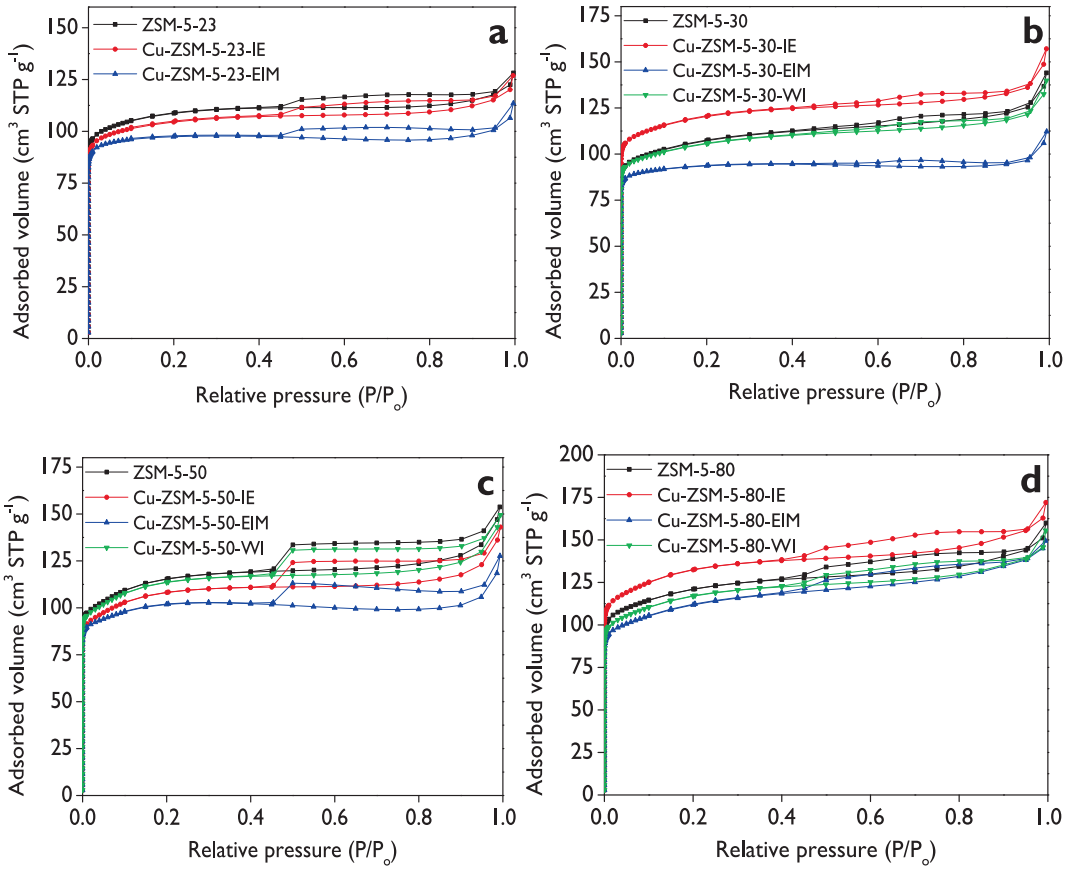

Fig. 3. N_2 adsorption–desorption isotherms of catalysts based on **(a)** ZSM-5-23, **(b)** ZSM-5-30, **(c)** ZSM-5-50, and **(d)** ZSM-5-80.

Fig. 4c and Table S7 show that strong Brønsted acidity dominates in the parent materials, representing the largest fraction of the total acidity with values of 71.9% and 75.8% corresponding to 381 and 262 μmol g^{-1} in ZSM-5–23 and ZSM-5–30, respectively. After Cu incorporation, this fraction decreases significantly, especially in samples prepared by evaporation impregnation method (EIM), where strong Brønsted acidity drops to 163 μmol g^{-1} (Cu-ZSM-5–23-EIM) and 61 μmol g^{-1} (Cu-ZSM-5–30-EIM). At the same time, a substantial increase in medium and strong Lewis sites is observed; for example, in Cu-ZSM-5-23-EIM, strong Lewis acidity reaches 226 μmol g^{-1}, while in Cu-ZSM-5-80-EIM it reaches 163 μmol g^{-1}, surpassing the corresponding strong Brønsted contribution (19 μmol g^{-1}). It is noteworthy that the catalysts prepared by ion exchange tend to retain a larger fraction of strong Brønsted sites, for instance: 328 μmol g^{-1} in Cu-ZSM-5-23-IE vs. 381 μmol g^{-1} in ZSM-5-23. In the case of Cu-ZSM-5-30-IE, the strong Brønsted acidity did not change regarding ZSM-5-30, with the same value of 262 μmol g^{-1}, while Cu-ZSM-5-50-IE slightly increased strong Brønsted acidity to 138 μmol g^{-1} from 101 μmol g^{-1} for ZSM-5-50. Overall, the EIM method favors predominantly strong Lewis acidity with BAS/LAS molar ratios (Fig. 4b, Table S7) of 0.5, 0.3, 0.2, and 0.1 for Cu-modified ZSM-5 with nominal SiO_2/Al_2O_3 molar ratios corresponding to 23, 30, 50, and 80, respectively.

Fig. 4d presents the ^{27}Al MAS NMR spectra of parent zeolites with different SiO_2/Al_2O_3 molar ratios and selected Cu-ZSM-5 catalysts. The spectra are dominated by a signal at ~55 ppm assigned to tetrahedrally coordinated framework Al (Al_{IV}), responsible for Brønsted acid sites (Al-OH-Si), while a weaker signal near 0 ppm corresponds to octahedrally coordinated extra-framework Al (Al_{VI}) [35–37]. The absence of resonance around 30 ppm indicates absence of five-coordinated extra-framework Al [38]. On the other hand, the ^{29}Si MAS NMR spectra (Fig. S10) show a main resonance between −112 and −115 ppm assigned to Q^4 $Si(OSi)_4$ units of the MFI framework, along with a shoulder at −100 to −105 ppm associated with Q^3 $Si(OSi)_3OH$ species related to defects and silanol groups [35].

In zeolite-catalyzed reactions, it is often assumed that an increased population of Al_{VI} species is directly associated with higher Lewis acidity [39,40]. Following this interpretation, a higher Al_{VI}/Al_{IV} ratio should correspond to a lower BAS/LAS ratio, implying an inverse relationship between these two descriptors. However, Fig. 4e shows the opposite tendency, as higher Al_{VI}/Al_{IV} values are accompanied by higher BAS/LAS ratios, i.e., a positive trend is observed. Despite this apparent linear behavior, it would be incorrect to interpret this as a dependent or causal relationship. The Al_{VI}/Al_{IV} ratio derived from ^{27}Al MAS NMR is a bulk structural descriptor that includes all octahedral Al species, regardless of accessibility, acidity, or chemical environment, whereas the BAS/LAS ratio obtained from pyridine-FTIR quantifies only pyridine-accessible surface acid sites [41]. Therefore, the positive trend in Fig. 4e reflects co-variation driven by framework perturbation, intrinsic dealumination, and Cu incorporation, rather than a direct structural-acidity correlation. This distinction is reinforced by the case of ZSM-5-30, which combines a relatively high Al_{VI}/Al_{IV} ratio (0.60) with a high BAS/LAS ratio (5.5), clearly demonstrating that octahedral Al content cannot be used as a quantitative predictor of measurable Lewis acidity.

Fig. 4e shows that ZSM-5-23 exhibits a high BAS/LAS ratio (10.3) together with a low Al_{VI}/Al_{IV} value (0.15), indicating that aluminum is predominantly preserved in tetrahedral framework positions and Brønsted acidity prevails. ZSM-5–30 shows more pronounced intrinsic dealumination, reflected in its higher Al_{VI}/Al_{IV} ratio, yet the BAS/LAS ratio remains high because a substantial fraction of extra-framework Al does not generate pyridine-accessible Lewis acid sites. Upon Cu incorporation, the observed decrease in Al_{VI}/Al_{IV} is consistent with re-coordination of extra-framework Al into Cu–O–Al species rather than reinsertion into the framework [42]. It should be noted, however, that for the catalysts with the highest Cu loadings, particularly those

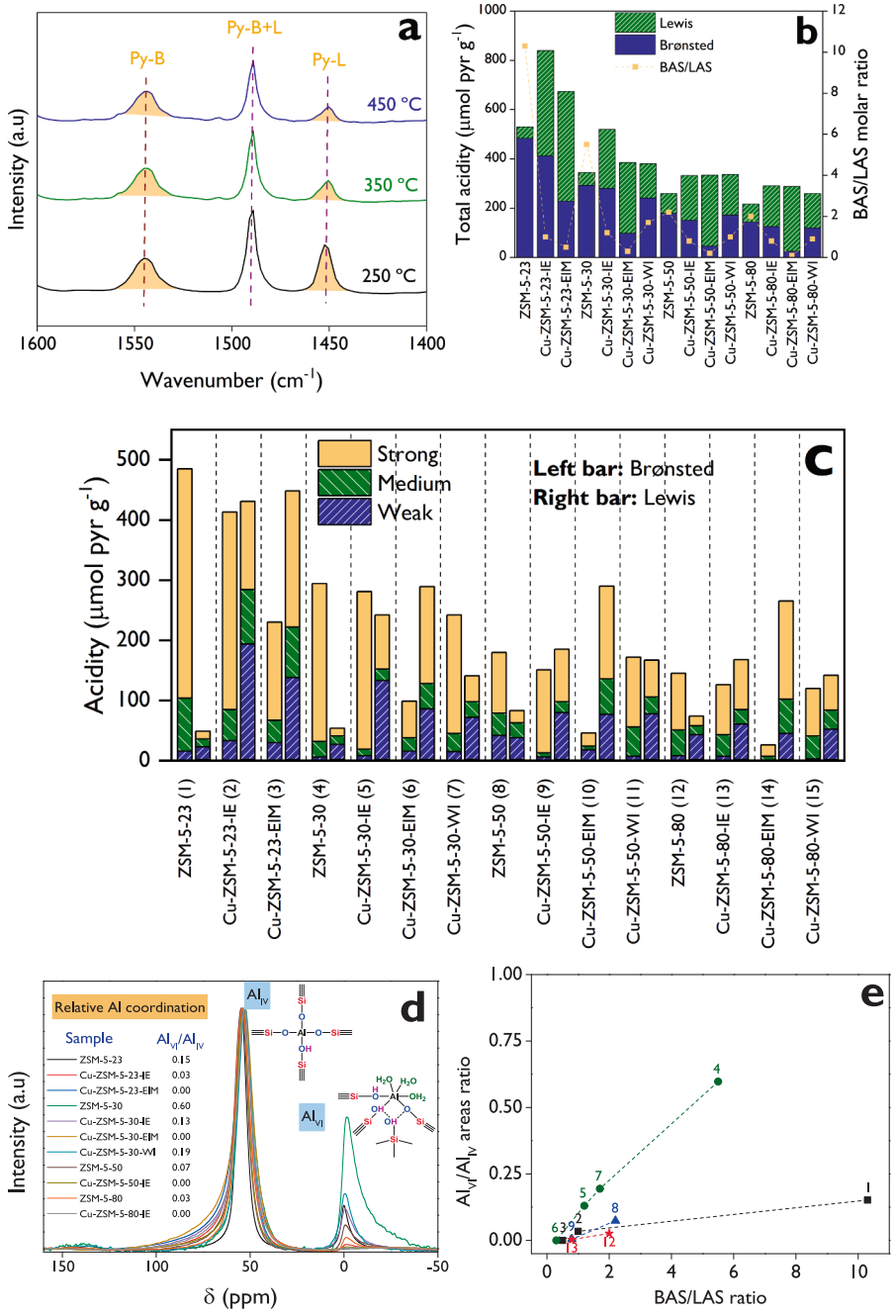

Fig. 4. A) Typical pyridine-adsorbed FTIR spectrum (Cu-ZSM-5-30-WI as an example), **b)** Total concentration of Brønsted and Lewis acid sites, and the Brønsted-to-Lewis molar ratios (BAS/LAS) for all the catalysts, **c)** Distribution of Brønsted (left bars) and Lewis (right bars) acid sites classified by strength (weak, medium, strong), calculated from pyridine-FTIR analysis. Measurements at 250 °C: weak + medium + strong; measurements at 350 °C: medium + strong; measurements at 450 °C: strong, **d)** Solid-state ^{27}Al MAS NMR spectra of parent zeolites with different SiO_2/Al_2O_3 molar ratios and selected Cu-ZSM-5 catalysts, normalized to the intensity of the tetrahedral Al(IV) resonance at ~55 ppm, **e)** Al_{VI}/Al_{IV} ratio vs. BAS/LAS ratio for catalysts based on ZSM-5-23 (–■–), ZSM-5–30 (–●–), ZSM-5–50 (–▲–), and ZSM-5-80 (–★–). The numbers in figure **e** correspond to the catalysts enumerated in the x-axis caption of figure **c**.

prepared by EIM ($Al_{VI}/Al_{IV} = 0.00$, Fig. 4d), the complete disappearance of the octahedral Al signal may be influenced by the paramagnetic nature of Cu^{2+} species, which are known to strongly interact with nearby nuclei, accelerating relaxation and broadening NMR signals, thereby reducing the observable intensity of specific Al environments without necessarily indicating a true structural loss of those species [43]. In the more siliceous ZSM-5–50 and ZSM-5-80 samples, lower Al_{VI}/Al_{IV} ratios indicate more framework stability, and only minor changes occur after Cu addition. In conclusion, Fig. 4e should be interpreted as illustrating parallel but fundamentally distinct responses of structural Al coordination and surface acidity to composition and metal incorporation, rather than a quantitative structural-acidity correlation.

3.4. Copper dispersion and reducibility

The dispersion and particle size of copper species on the ZSM-5 catalysts were initially investigated by transmission electron microscopy (TEM). Representative micrographs and the corresponding Cu particle size distributions are shown in Fig. 5. A key and systematic observation is that the largest Cu particles are found exclusively in

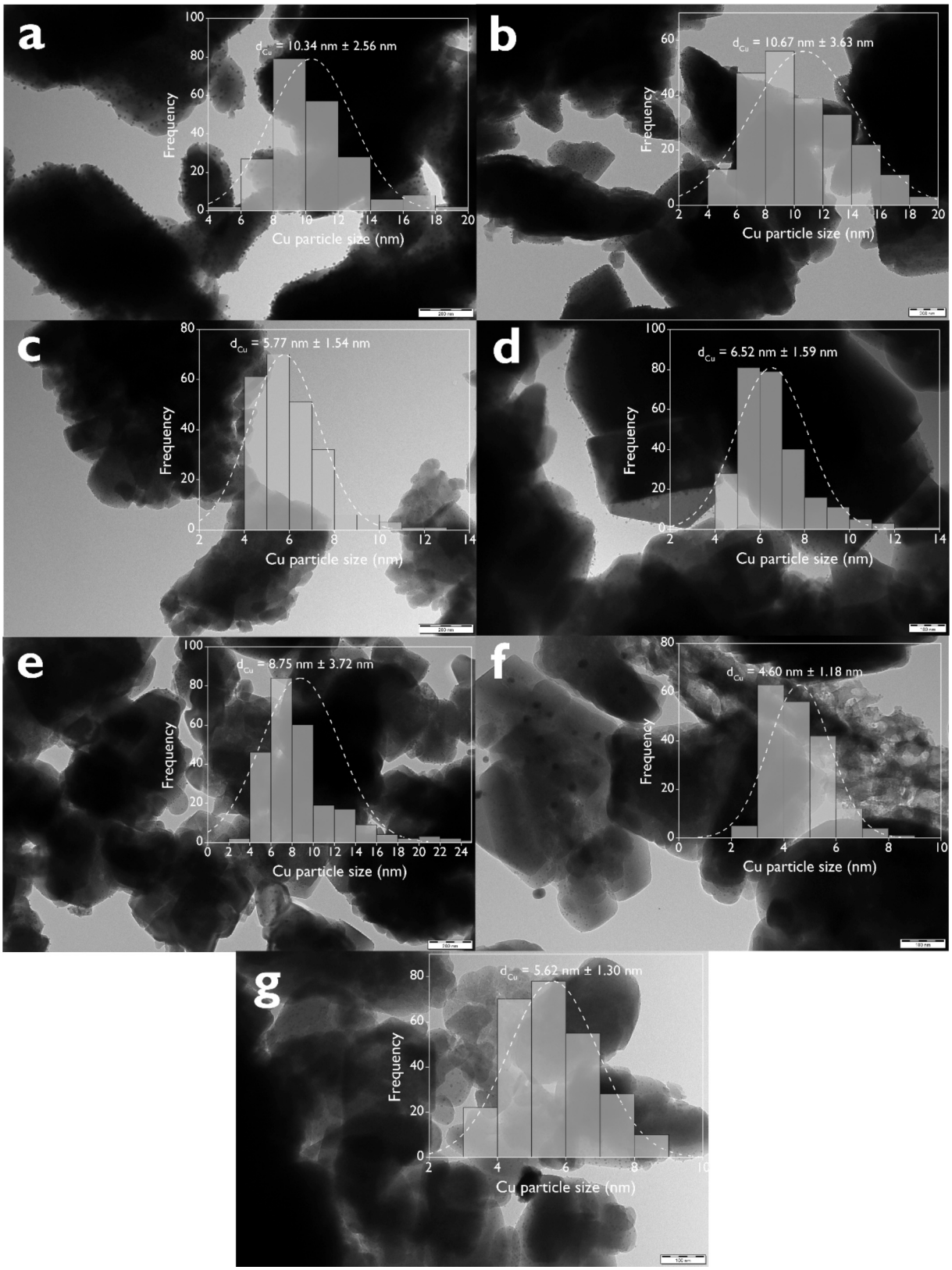

Fig. 5. TEM micrographs and particle size distributions of **a)** Cu-ZSM-5-23-IE, **b)** Cu-ZSM-5-23-EIM, **c)** Cu-ZSM-5-30-EIM, **d)** Cu-ZSM-5-50-WI, **e)** Cu-ZSM-5-50-EIM, **f)** Cu-ZSM-5-80-WI, **g)** Cu-ZSM-5-80-EIM. The ruler sizes for the images are 200 nm (**a, b, c, e**) and 100 nm (**d, f, g**).

catalysts based on ZSM-5-23. In particular, Cu-ZSM-5-23-IE (Fig. 5a) and Cu-ZSM-5-23-EIM (Fig. 5b) exhibit mean Cu particle sizes of approximately 10–11 nm, which are significantly larger than those observed for catalysts with higher Si/Al ratios (Fig. 5c–g), regardless of the Cu introduction method, with mean sizes ranging from 4.6 to 8.8 nm. This behavior indicates that the zeolite framework composition plays a dominant role in governing Cu aggregation. Solid-state ^{27}Al MAS NMR showed that the parent ZSM-5–23 zeolite contains a relatively high fraction of extra-framework aluminum ($Al_{VI}/Al_{IV} = 0.15$, Fig. 4d), which is largely removed upon Cu incorporation ($Al_{VI}/Al_{IV} = 0.03 - 0.00$, Fig. 4d), suggesting the formation of Cu–O-Al species as reported in the literature for Cu-exchanged mordenite [42], restoring a framework dominated by tetrahedral Al. This high density of accessible exchange sites in ZSM-5-23, combined with Cu loadings of 2.4–4.1 wt% (Table 1), leads to local saturation of anchoring positions during Cu introduction and promotes the formation of excess Cu species that agglomerate into the large particles observed by TEM. In contrast, ZSM-5 with higher Si/Al ratios, despite comparable Cu loadings, exhibits predominantly small clusters as observed for Cu-ZSM-5-30-EIM (3.6 wt% Cu, Fig. 5c), Cu-ZSM-5-50-EIM (3.2 wt% Cu, Fig. 5e), and Cu-ZSM-5–80-EIM (3.2 wt% Cu, Fig. 5g) with mean Cu sizes of 5.8 nm, 8.8 nm, and 5.6 nm, respectively. Nevertheless, these values are still much larger than the average pore size (0.6 nm, Fig. S8).

Moreover, catalysts prepared by wetness impregnation with lower Cu loadings (Table 1) lead to relatively smaller particles, with mean Cu particle sizes of 6.5 nm for Cu-ZSM-5–50-WI (0.6 wt% Cu, Fig. 5d) and 4.6 nm for Cu-ZSM-5-80-WI (0.5 wt% Cu, Fig. 5f). This behavior is in line with the trend observed for ZSM-5-23, demonstrating that higher framework Si/Al ratios favor lower Cu particle sizes. On the other hand, in several catalysts (Cu-ZSM-5-30-IE, Cu-ZSM-5-30-WI, and Cu-ZSM-5-80-IE) with Cu loadings below 0.7 wt% (Table 1), the direct identification of Cu nanoparticles is challenging, either because of the very small Cu particle size, the low metal loading, or the limited contrast between finely dispersed Cu species and the zeolitic support, as is observed in Fig. S11.

The Cu dispersion (%), $D_{Cu,TEM}$, calculated from the mean Cu particle sizes determined by TEM (d_{TEM}), is presented in Table 2 for all the catalysts shown in Fig. 5. From Eq. (S1), it is evident that the dispersion is inversely proportional to d_{TEM}, which explains why the highest dispersion (22.5%), observed for Cu-ZSM-5-80-WI, corresponded to the lowest d_{TEM} (4.6 nm, Fig. 5f), whereas the lowest dispersions (9.7% and 10.0%) were found for catalysts based on ZSM-5-23 with the highest d_{TEM}. The other catalysts exhibited intermediate values, ranging from 9.7% to 22.5%.

While $D_{Cu,TEM}$ provides a geometric estimate based on particle size distributions, this approach assumes spherical particles and complete detectability by TEM. However, as discussed in the Supporting Information (Section 14), TEM may underestimate highly dispersed Cu species or ultrasmall Cu clusters due to limited contrast and sampling constraints. Therefore, to obtain a quantitative measure of the chemically accessible Cu surface, dispersion was independently determined by N_2O chemisorptive oxidation.

The s-TPR profiles of the Cu_2O phase obtained after N_2O oxidation (step 3) for selected catalysts are illustrated in Fig. 6a. The parent ZSM-5 samples (ZSM-5–23 and ZSM-5–30) did not show H_2 uptake over the entire temperature range, confirming the absence of reducible Cu species. In contrast, all Cu-containing catalysts, except Cu-ZSM-5–30-WI, exhibited distinct low-temperature H_2 consumption peaks, typically in the range of 110–155 °C, which are attributed to the reduction of surface Cu_2O species formed via selective oxidation of Cu^0 by N_2O, as reported in the literature [44]. For Cu-ZSM-5-23-IE, a sharp reduction peak centered at ca. 110 °C is observed, indicating the presence of easily reducible Cu_2O species. A similar but slightly shifted peak appears for Cu-ZSM-5-23-EIM at 129 °C, suggesting somewhat stronger Cu-support interactions, or a broader distribution of Cu particles as observed by TEM (Fig. 5b), which showed a high standard deviation (3.6 nm), resulting in a very high coefficient of variation (34%). The catalyst prepared by EIM with a nominal SiO_2/Al_2O_3 molar ratio of 30 exhibits a maximum peak at nearly the same temperature (126 °C); however, the dispersion values ($D_{Cu,N2O}$, Table 2) differ significantly, with values of 0.9% and 2.2% for Cu-ZSM-5-23-EIM and Cu-ZSM-5-30-EIM, respectively. Interestingly, Cu-ZSM-5-30-IE and Cu-ZSM-5-50-IE, both prepared by ion-exchange, exhibit the strongest Cu-support interactions, as indicated by maximum peaks around 150 °C. However, the latter shows the lowest dispersion (0.5%), whereas the former exhibits the highest dispersion (4.6%), which is directly associated with the peak areas presented in Fig. 6a. Furthermore, a general trend toward higher Cu dispersion on ZSM-5–23 and ZSM-5-30 is observed at somewhat lower Cu loadings (Table 2). Overall, these dispersion values are consistent with those typically reported for Cu supported on silica, titania, and zirconia using this method, with values between 4.8% and 5.8% [44]. All dispersion values determined by the N_2O oxidation method are approximately one order of magnitude lower than those estimated by TEM, highlighting the severe limitations of TEM for accurately determining Cu dispersion, as previously discussed.

For comparative purposes, Cu dispersion was also estimated from H_2 consumption during conventional H_2-TPR experiments, following Eq. (S4). Accordingly, the corresponding profiles are presented in Fig. 6b. As

Table 2
Copper dispersion of selected ZSM-5 catalysts determined by different methods.

Method	Cu (wt.%)	TEM		N_2O		TPR	
Catalyst		d_{TEM} (nm)	$D_{Cu,\ TEM}$ (%)	H_2 (mmol/g)[a]	$D_{Cu,\ N2O}$ (%)	H_2 (mmol/g)[b]	$D_{Cu,\ TPR}$ (%)
Cu-ZSM-5-23-IE	2.4	10.3	10.0	0.0024	1.3	0.397	1.2
Cu-ZSM-5-23-EIM	4.1	10.7	9.7	0.0029	0.9	0.391	1.5
Cu-ZSM-5-30-IE	0.6	np	np	0.0022	4.6	0.038	11.2
Cu-ZSM-5-30-WI	0.4	np	np	nd	nd	0.015	nc
Cu-ZSM-5-30-EIM	3.6	5.8	18.0	0.0062	2.2	0.357	3.5
Cu-ZSM-5-50-IE	0.9	na	na	0.0004	0.5	0.011	6.9
Cu-ZSM-5-50-WI	0.6	6.5	15.9	na	na	na	na
Cu-ZSM-5-50-EIM	3.2	8.8	11.8	na	na	na	na
Cu-ZSM-5-80-WI	0.5	4.6	22.5	na	na	na	na
Cu-ZSM-5-80-EIM	3.2	5.6	18.4	na	na	na	na

d_{TEM} is the average particle diameter from the particle size distributions (Fig. 5); $D_{Cu,TEM}$ was calculated by Eq. (S1); $D_{Cu,N2O}$ was calculated by Eq. (S2); $D_{Cu,TPR}$ was calculated by Eq. (S4).
np: no particles observed in TEM (Fig. S11).
nd: no detectable signal for Cu-ZSM-5–30-WI (Fig. 6a).
nc: not calculated due to no detectable signal (nd).
na: not analyzed.
[a] H_2 consumption from areas in Fig. 6a using Eq. (S3) ($\beta = 15$ °C min^{-1}).
[b] H_2 consumption from areas in Fig. 6b using Eq. (S3) ($\beta = 10$ °C min^{-1}).

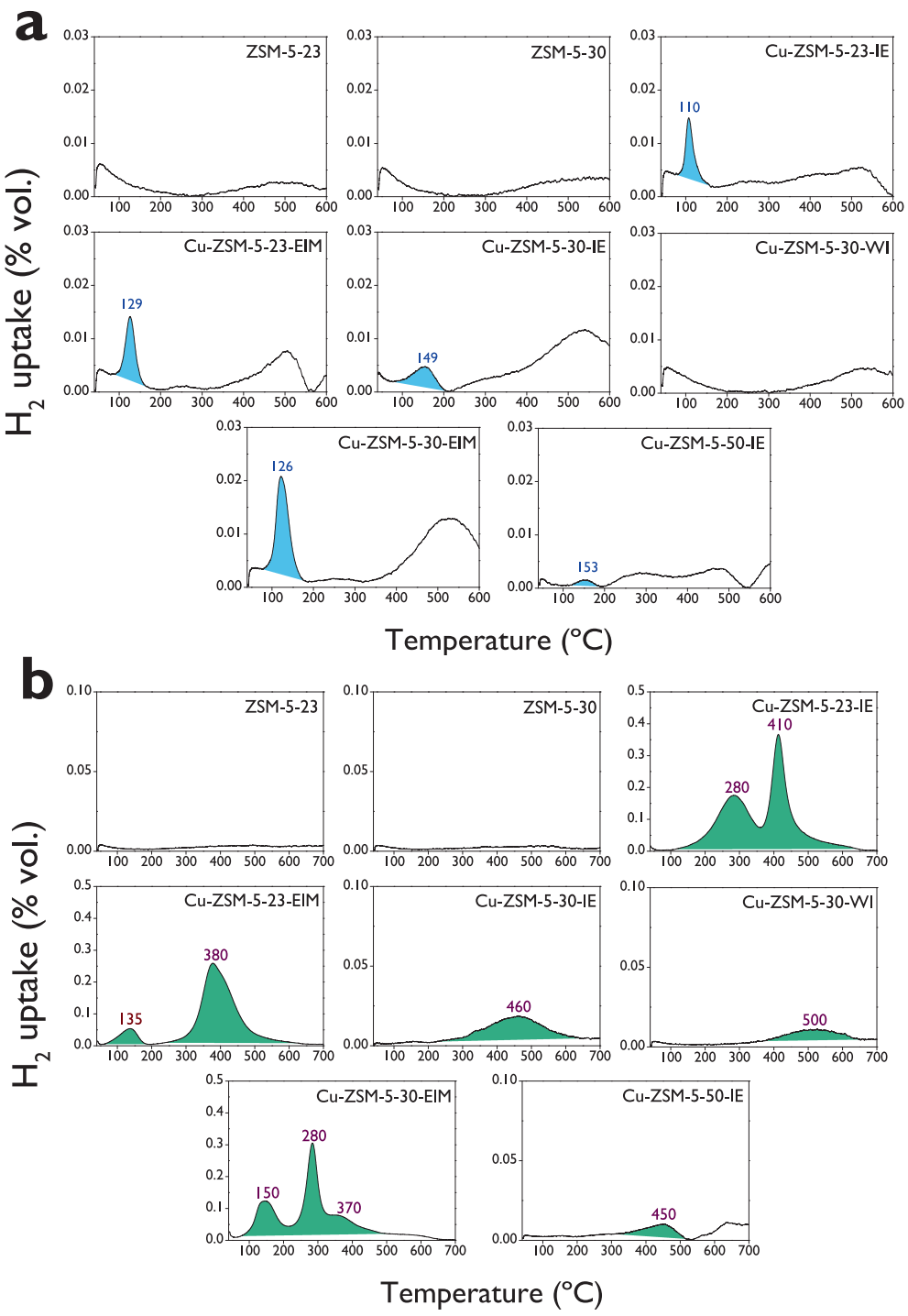

Fig. 6. S-tpr profiles of the cu_2O phase obtained after N_2O oxidation (step 3) **(a)** and H_2-TPR profiles **(b)** for selected catalysts.

expected, the parent ZSM-5 samples do not exhibit any detectable H_2 uptake, confirming the absence of reducible species. In contrast, all Cu-based catalysts display reduction features over a wide temperature range (≈ 120–600 °C), which are characteristic of multistep reduction processes involving $Cu^{2+} \rightarrow Cu^{+} \rightarrow Cu^{0}$ transitions [45,46]. The reduction of two types of isolated Cu^{2+} species at the ion-exchange sites of zeolites, namely Cu^{2+}-2Z and $[Cu(OH)]^{+}$-Z (Z referring to zeolite), occurs at different temperatures due to their different stabilities in zeolites. The reduction of the more stable Cu^{2+}-2Z species to Cu^{+} has been reported to occur at ≈ 400 °C, whereas the less stable $[Cu(OH)]^{+}$-Z species are reduced at ≈ 250 °C [46–48]. A further reduction peak of Cu^{+} to Cu^{0} has been reported at ≈ 360 °C [46]. Furthermore, the reduction of CuO nanoparticles in Cu-based zeolites is much easier than that of Cu cations, as they can be directly reduced to Cu^{0} at around 300 °C [46,49]. Additionally, in some Cu-supported zeolites, a reduction peak at around 700–900 °C can be observed, which has been attributed to the reduction of Cu^{+} species at the ion-exchange sites. In this case, strong interactions between the zeolite framework and Cu^{+} species hinder the reduction process [46].

From Fig. 6b, the presence of $[Cu(OH)]^{+}$-Z species is clearly observed in two catalysts with high Cu loadings, namely Cu-ZSM-5-23-IE and Cu-ZSM-5-30-EIM, as indicated by the maximum peak at ca. 280 °C. On the other hand, catalysts with Cu loadings below 1 wt% (Table 1), such as Cu-ZSM-5-30-IE, Cu-ZSM-5-30-WI, and Cu-ZSM-5-50-IE, exhibit only

one reduction feature, which is associated with the stable Cu^{2+}-2Z species, with maximum peaks between 450 and 500 °C. Additionally, the Cu-ZSM-5-23-IE catalyst exhibits a sharp maximum peak around 410 °C, which can also be associated with this stable species. These results are completely in agreement with the observations of Song et al. [50], confirming that in catalysts with low Si/Al ratios and low Cu loadings, Cu^{2+}-2Z species predominate. The peak observed around 370–380 °C in the catalysts prepared by EIM can be associated with an overlap of Cu^{2+}-2Z species and CuO nanoparticles, which is consistent with the high Cu loadings of these catalysts (3.6 wt% and 4.1 wt%, Table 1). Additionally, the first peak observed at 100–150 °C for these two catalysts is attributed to the reduction of surface CuO clusters located on the external surface of the zeolite framework, as reported by Liu et al. for Cu/SAPO-34 catalysts [51].

The dispersion values derived from H_2 consumption during conventional H_2-TPR ($D_{Cu,TPR}$), shown in Table 2, are apparently comparable to those obtained by the N_2O oxidation method ($D_{Cu,N2O}$), differing by less than a factor of two for all catalysts, as previously reported in the literature for Cu-supported catalysts [44], except for Cu-ZSM-5-50-IE. For this catalyst, the large discrepancy (0.5% vs. 6.9%) arises from the very low H_2 consumption (0.011 mmol g^{-1}, Table 2), indicating a low concentration of reducible Cu species. Therefore, comparable dispersion values from both methods can only be expected when all Cu species are accessible and fully reduced to Cu^0. Consequently, the N_2O oxidation method provides the most reliable measure of Cu dispersion, as it selectively quantifies the true fraction of surface-accessible Cu.

3.5. Copper species

The UV–Vis–DRS spectra (Fig. 7) provide further insight into the nature and distribution of Cu species within the ZSM-5 framework and are fully consistent with the H_2-TPR results. The parent ZSM-5-30 sample exhibits high reflectance across the entire UV–visible region, confirming the absence of reducible metal species. Upon Cu introduction, all Cu-ZSM-5 catalysts show strong absorption below 300 nm, which is attributed to ligand-to-metal charge transfer (LMCT) transitions associated with isolated Cu^{2+} ions located at ion-exchange sites [46,52].

For the low-Cu-loaded catalysts (Cu-ZSM-5-30-IE and Cu-ZSM-5-30-WI), the spectra are characterized by relatively narrow bands in the UV region (green zone, Fig. 7) together with a subtle shoulder centered at ca. 280 nm (yellow zone, Fig. 7). This feature is assigned to LMCT transitions of isolated Cu^{2+} species residing in slightly different and less symmetric coordination environments, reflecting a limited heterogeneity within the population of framework-associated Cu^{2+} ions [46]. Notably, these two catalysts exhibit non-zero Al_{VI}/Al_{IV} ratios (0.13 and 0.19, Fig. 4d), as determined by solid-state ^{27}Al MAS NMR, indicating the presence of extra-framework Al species that can locally perturb the coordination environment of Cu^{2+} ions and give rise to the observed shoulder. In addition, a weak absorption band around 545 nm (cyan zone, Fig. 7) is observed for these samples, which is consistent with low-intensity d-d transitions of well-dispersed Cu^{2+} ions in strongly distorted, nearly square-planar coordination at ion-exchange sites [46,53]. Therefore, the predominance of isolated Cu^{2+}-2Z species inferred from UV–Vis-DRS is fully consistent with the single high-temperature reduction feature observed in H_2-TPR profiles (450–500 °C), Fig. 6b.

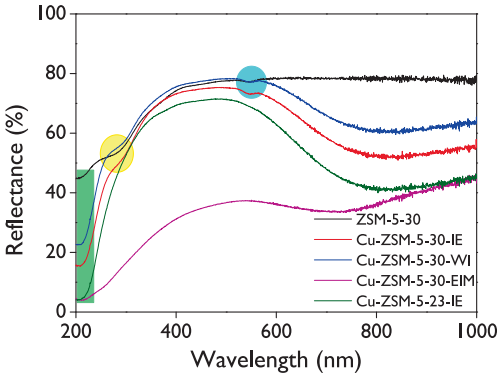

Fig. 7. UV–Vis-DRS spectra of selected catalysts.

In contrast, both Cu-ZSM-5-23-IE and Cu-ZSM-5-30-EIM exhibit broader absorption extending into the visible region (300–600 nm), together with a pronounced decrease in overall reflectance, evidencing a wider distribution of Cu coordination environments. For these catalysts, the absence of the ~280 nm shoulder indicates the lack of a well-defined population of isolated Cu^{2+} species in slightly distorted framework environments, as can be correlated with Al_{VI}/Al_{IV} ratios lower than 0.03 (Fig. 4d), indicating poor extra-framework Al species and a fundamentally different Cu–Al interaction compared with Cu-ZSM-5-30-IE and Cu-ZSM-5–30-WI. On the other hand, the broad visible bands are characteristic of contributions from less stable $[Cu(OH)]^+$-Z species and small CuO-like domains or surface clusters, which generate stronger visible absorption and are more easily reduced at lower temperature in H_2-TPR (appearance of peaks at ~280 °C and 100–150 °C, Fig. 6b) [46,54,55]. Overall, the UV–Vis-DRS results corroborate the TPR analysis, demonstrating that low Cu loadings favor isolated and stable Cu^{2+} species, whereas increasing Cu content leads to the formation of multiple Cu environments with reduced stability and lower dispersion.

3.6. Turnover frequency (TOF) as a descriptor of catalytic activity

The catalytic performance of the prepared Cu-modified zeolites was investigated in the direct oxidation of methane to methanol (DOMTM) using H_2O_2 as an oxidant and water as a green solvent, under mild temperature (50 °C). TOF, as a measure of the catalytic activity for the production of methanol, was calculated based on the total acidity (TOF_A, Eq. (8)) and the Cu dispersion (TOF_D, Eq. (9)). Those values have been correlated with the Cu dispersion (Fig. 8a and 8b), the Brønsted-to-Lewis (BAS/LAS) molar ratio (Fig. 8c and d, Fig. S12a), and the Brønsted acid site density (Fig. 8e and f, Fig. S12b). According to Fig. 8a, b, d, and f, the Cu-ZSM-5-30-IE catalyst exhibited the highest TOF values with values of $TOF_A = 3.3\ h^{-1}$ and $TOF_D = 399.6\ h^{-1}$, which exhibited the highest Cu dispersion (4.6%, Table 2). However, Fig. 8c and e showed that the Cu-ZSM-5-30-WI catalyst exhibited slightly higher TOF_A value than Cu-ZSM-5-30-IE, with a value of $4.3\ h^{-1}$. However, the TOF_D could not be determined for this catalyst (Table 2) because Cu dispersion could not be estimated from the s-TPR profile (Fig. 6a), as no detectable feature was observed. On the other hand, Fig. 8c and e reveal the existence of a maximum in TOF_A as a function of both the BAS/LAS molar ratio and the Brønsted acid site density across the Cu-ZSM-5 catalyst series, which is essentially governed by the nominal SiO_2/Al_2O_3 molar ratio.

The two highest TOF_A values with the ZSM-5-30 series are reached at BAS/LAS = 1.2 and 1.7 for Cu-ZSM-5–30-IE ($3.3\ h^{-1}$) and Cu-ZSM-5–30-WI ($4.3\ h^{-1}$), respectively. In contrast, with the ZSM-5-23 series, the highest TOF_A value is reached at BAS/LAS = 1.0 for Cu-ZSM-5-23-IE ($0.9\ h^{-1}$). Regarding the Brønsted acid site density (Fig. 8e), the maximum values are reached at 0.58, 0.57, and 0.96 μmol m^{-2} for Cu-ZSM-5–30-IE, Cu-ZSM-5-30-WI, and Cu-ZSM-5–23-IE, respectively. On the other hand, all ZSM-5-50 and ZSM-5-80 catalyst series exhibited very poor catalytic activity for producing methanol, as demonstrated in Figs. S12a and S12b. Although some of these materials displayed BAS/LAS ratios within the range observed for the most active catalysts (1.0–1.7), all of them exhibited Brønsted acid site densities below the previously identified lower limit (0.58–0.96 μmol m^{-2}). Furthermore, because the BAS/LAS ratio and the Al_{VI}/Al_{IV} ratio vary concomitantly as a function of the framework zeolite composition and Cu loading (Fig. 4e), TOF_A and TOF_D exhibit similar trends when plotted as a function of the Al_{VI}/Al_{IV} ratio (Figs. S12c and S12d), reaching maximum values at 0.19 and 0.13 for Cu-ZSM-5-30-WI and Cu-ZSM-5-30-IE, respectively. Interestingly, TOF_D as a function of BAS/LAS ratio

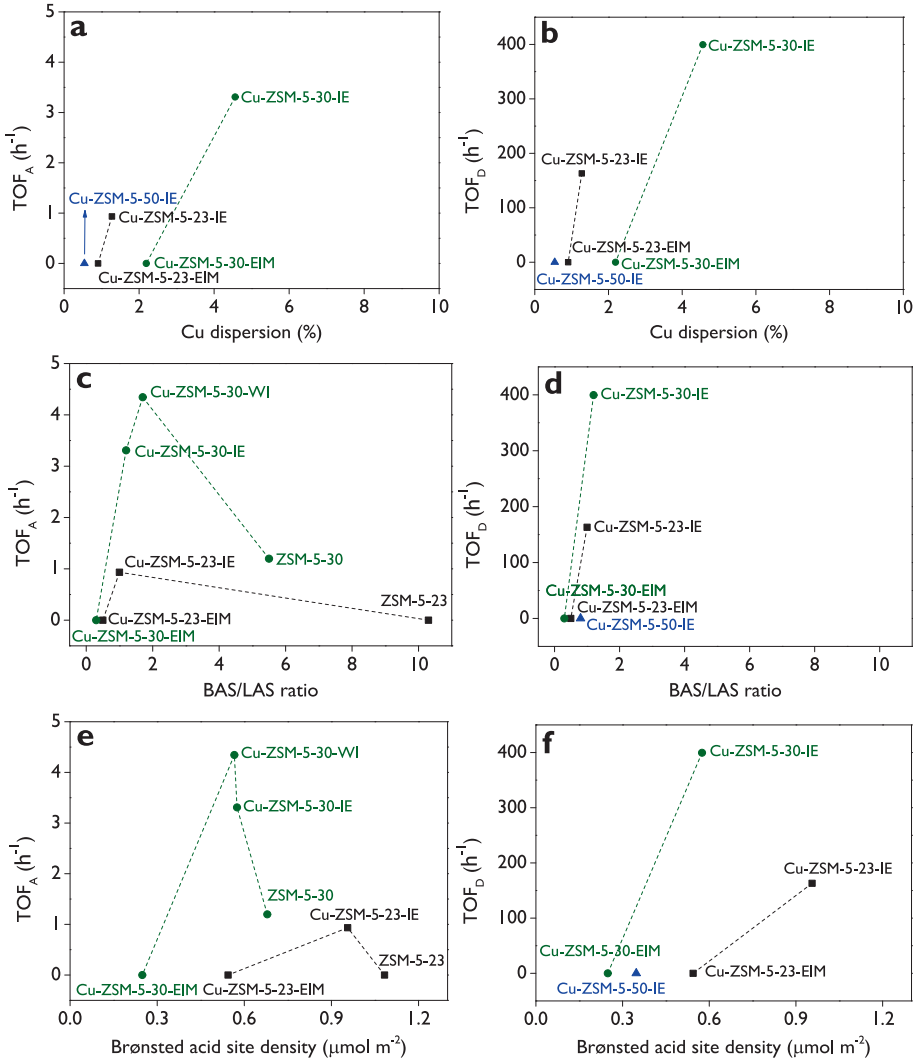

Fig. 8. Turnover frequency (TOF) of methanol in the DOMTM route over ZSM-5-based catalysts, calculated based on the **(a, c, e)** total acidity (TOF_A) and **(b, d, f)** Cu dispersion (TOF_D), as a function of **(a, b)** Cu dispersion, **(c, d)** BAS/LAS molar ratio, and **(e, f)** Brønsted acid site density. **Reaction conditions:** 30 bar CH_4 at room temperature, 0.5 mol L^{-1} H_2O_2 in deionized water, 70 mL total volume, 150 mg catalyst, 50 °C, 1000 rpm.

(Fig. 8d) and the Al_{VI}/Al_{IV} ratio (Fig. SI2d) exhibits a positive linear trend that is nearly independent of the nominal SiO_2/Al_2O_3 molar ratio.

For the first time, this work reports correlations between TOF values, calculated based on total acidity and Cu dispersion, and key physicochemical descriptors of zeolitic catalysts, such as Cu dispersion, BAS/LAS ratio, and Brønsted acid site density, as shown in Fig. 8. Because this type of plots has not been previously reported, direct benchmarking against the literature required calculating TOF using the conventional definition employed in the recent DOMTM studies, i.e., mol of oxygenated products per mol of metal per unit time (Fig. 9). Using this definition, the catalysts prepared in this work exhibit performances comparable to those previously reported for the DOMTM route, with values of 16 h^{-1} and 22 h^{-1} for Cu-ZSM-5-30-IE and Cu-ZSM-5-3-WI, respectively, and CH_3OH selectivities between 45 and 55%. In contrast, CuFe/ZSM-5-30 [11] reaches a methanol selectivity as high as 85% at a TOF of 31 h^{-1}, while Cu(1.25)Fe/ZSM-5 [56] displays a higher activity (45 h^{-1}) at a selectivity of 78%. CuFe/ZSM-5-30 [11] was prepared via solid-state ion exchange using a ZSM-5 support with a SiO_2/Al_2O_3 molar ratio ≈ 30 and 2.5 wt% Fe, but the metal dispersion was not reported. In contrast, Cu(1.25)Fe/ZSM-5 [56] was prepared with equal Cu and Fe loadings (1.25 wt% each) on a ZSM-5 support with a lower SiO_2/Al_2O_3 ratio of 23, yet dispersion data were again omitted. Cu-Fe (0.1/0.1)/ZSM-5 [8] achieves substantially higher activity (134 h^{-1}),

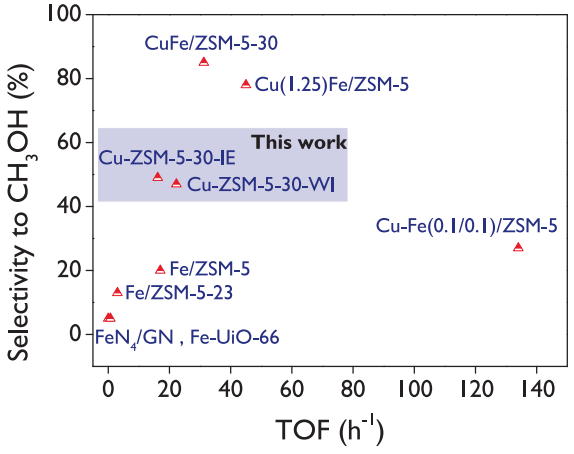

Fig. 9. Comparison of selectivity to CH_3OH vs. turnover frequency (TOF, mol products/(mol metal × time)) for recent heterogeneous catalysts reported for the DOMTM route. CH_4 conversions are generally below 1%.

but at the expense of CH_3OH selectivity (27%). For comparison, Fe-based catalysts, including Fe/ZSM-5 [57], Fe/ZSM-5-23 [56], FeN_4/

GN [58], and Fe-UiO-66 [59], typically display TOF values below 20 h^{-1} and methanol selectivities lower than 20%, confirming the competitive performance of the Cu-ZSM-5 catalysts investigated here.

Although Cu-Fe bimetallic catalysts outperform monometallic systems in terms of activity, the objective of this study was not catalyst optimization but a systematic structure-performance analysis. In this context, Cu-ZSM-5 is an appropriate model catalyst, as it allows the effects of acidity, metal dispersion, and acid site distribution to be isolated without the synergistic influence of metal–metal interactions. This approach enables a suitable interpretation of the catalytic trends governing methanol formation in the DOMTM route.

3.7. Conversion of methane to oxygenated products

The methane conversion profiles toward oxygenated products (CH_3OOH, CH_3OH, and HCOOH), detected by HPLC up to 4 h, are presented in Fig. 10 for the catalyst families with nominal SiO_2/Al_2O_3 ratios of 23 (Fig. 10a) and 30 (Fig. 10b). The corresponding data for the higher SiO_2/Al_2O_3 ratios (50 and 80) are presented in the Supporting Information (Fig. S13), as these materials exhibited significantly lower activity to methanol, consistent with the TOF analysis discussed in Fig. 8 and Fig. S12. Although conversion profiles are not commonly reported in studies on methane to methanol conversion due to the very low CH_4 conversion values, it is considered highly relevant to report all catalytic performance parameters in order to achieve a better understanding of this challenging route. The conversion profiles are strongly dependent on both the zeolite composition and the Cu introduction method due to different physicochemical properties such as dispersion, BAS/LAS, and Brønsted acid site density, as was previously discussed in the TOF measurements (Fig. 8, Fig. S12).

The ZSM-5-23 series (Fig. 10a) exhibits low activity, regardless of Cu incorporation, showing conversions of 0.10% and 0.12% after 4 h for the ZSM-5-23 support and Cu-ZSM-5-23-IE catalyst, respectively. In contrast, the Cu-ZSM-5-30 catalysts (Fig. 10b) prepared by ion-exchange and wetness impregnation display the highest conversions (0.39% and 0.35%, respectively) among all the prepared catalysts, with a nearly linear increase in CH_4 conversion over the reaction time. For higher SiO_2/Al_2O_3 ratios (50 and 80), all Cu-containing catalysts exhibited poor activity (Figs. S13a and S13b), with the CH_4 conversion after 4 h decreasing in the following order: Cu-ZSM-5-50-IE (0.12%) > Cu-ZSM-5–50-WI (0.11%) > Cu-ZSM-5–50-EIM (0.01%), and Cu-ZSM-5–80-IE (0.03%) = Cu-ZSM-5–80-WI (0.03%) > Cu-ZSM-5-80-EIM (0.01%). All these catalysts exhibited BAS/LAS ratios below 1.0 (Fig. 4b, Table S7). Those conversion values are lower than the CH_4 conversions achieved with the parent zeolites, which reach 0.19% and 0.26% for ZSM-5-50 and ZSM-5-80 (Fig. S13), respectively. This could be explained by the higher BAS/LAS ratios (2.2 and 2.0 for ZSM-5-50 and ZSM-5-80, respectively) observed within these catalyst families (Fig. 4b, Table S7), highlighting the critical role of the balance of Brønsted and Lewis acidity in the conversion of methane. Additionally, the reaction was conducted without a catalyst (blank) to demonstrate that the reaction showed negligible activity.

Furthermore, it is noteworthy that all the catalysts prepared by EIM (Fig. 10, Fig. S13), regardless of the nominal SiO_2/Al_2O_3 ratio, remain essentially inactive for methane activation. This behavior is explained by the H_2O_2 conversion profiles (Fig. S14), which show very high values after 4 h, ranging from 60 to 87%. This is attributed to high Cu loadings (>3.2%) in these catalysts (Table 1, Fig. S14e), indicating that they strongly favor a competitive route in the liquid phase, such as the H_2O_2 decomposition [60], rather than methane oxidation. Additionally, the large CuO nanoparticles located on the external surface of EIM catalysts (5.6–8.8 nm, Table 2 and Fig. 5) likely promote radical recombination before •OH species can reach the internal active sites, further hindering the reaction.

In conclusion, methane conversion to oxygenated products remains below 0.4% for all samples, excluding contributions from formaldehyde and CO_2, reflecting the inherently low conversions reported by Hammond et al. [11] (0-0.7%). Thus, the total methane conversion is higher and will be discussed later. In this context, the values obtained in this work are comparable to those of state-of-the-art catalysts.

3.8. Product distribution

The selectivity to methyl hydroperoxide (CH_3OOH) as a function of methane conversion (X_{OP}) over ZSM-5–based catalysts is presented in Fig. 11 for catalyst series with SiO_2/Al_2O_3 = 23 and 30, while the profiles for the less active catalysts with higher SiO_2/Al_2O_3 ratios are provided in the Supporting Information (Fig. S15). Fig. 11 provides a clear mechanistic evidence that CH_3OOH is a primary intermediate in the oxidation of methane to methanol, as represented in Fig. 1a. The trends showed very high CH_3OOH selectivities, reaching values close to 100% at the beginning of the reaction, i.e., near-zero CH_4 conversion, indicating that the initial C–H activation of methane in the presence of H_2O_2 proceeds through the formation of the hydroperoxide species rather than directly yielding methanol or over-oxidized products (Fig. 1a). As the CH_4 conversion increased, a monotonic decrease in CH_3OOH selectivity was observed in all cases, independently of the Si/Al ratio and the catalyst preparation method, which is characteristic of an intermediate that is progressively consumed as the reaction proceeds. This behavior is expected from the reaction network presented in Fig. 1a, in which the chemical reactivity of CH_3OOH under the tested reaction conditions leads to methanol formation (Fig. 12) via O-O bond cleavage, as well as to further oxidation toward other oxygenated products.

The comparison between the parent ZSM-5 and the Cu-modified samples indicates that the presence of Cu species accelerates the conversion of CH_3OOH, as reflected by the lower selectivities observed

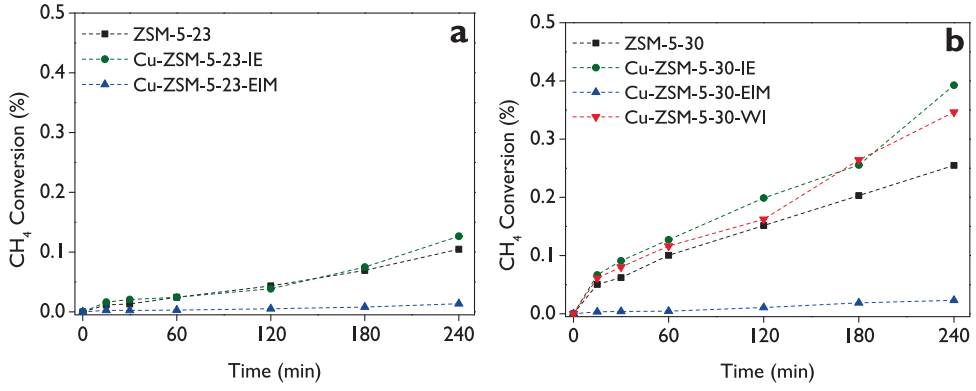

Fig. 10. Methane conversion to oxygenated products (X_{OP}) in the DOMTM route with H_2O_2 as an oxidant over catalysts based on **(a)** ZSM-5-23, and **(b)** ZSM-5-30. **Reaction conditions:** 30 bar CH_4 at room temperature, 0.5 mol L^{-1} H_2O_2 in deionized water, 70 mL total volume, 150 mg catalyst, 50 °C, 1000 rpm.

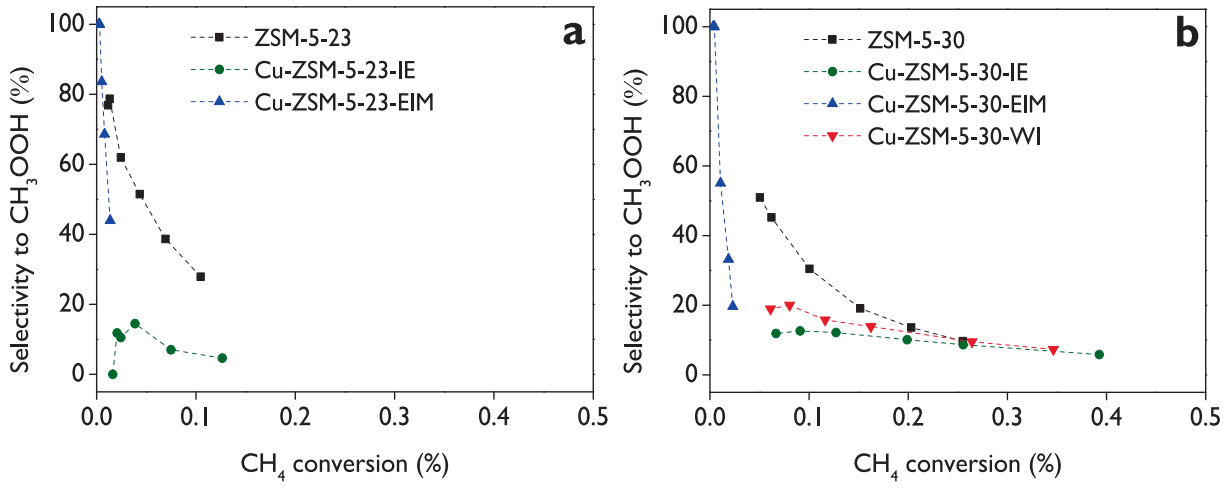

Fig. 11. Selectivity to methyl hydroperoxide (CH_3OOH) as a function of the CH_4 conversion to oxygenated products (X_{OP}) in the DOMTM route with H_2O_2 over catalysts based on **(a)** ZSM-5-23, and **(b)** ZSM-5-30. **Reaction conditions:** 30 bar CH_4 at room temperature, 0.5 mol L^{-1} H_2O_2 in deionized water, 70 mL total volume, 150 mg catalyst, 50 °C, 1000 rpm.

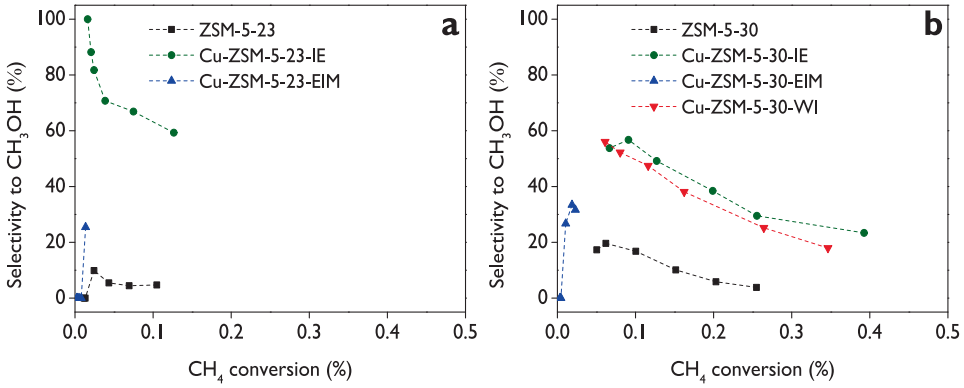

Fig. 12. Selectivity to methanol (CH_3OH) as a function of the CH_4 conversion to oxygenated products (X_{OP}) in the DOMTM route with H_2O_2 over catalysts based on **(a)** ZSM-5-23, and **(b)** ZSM-5-30. **Reaction conditions:** 30 bar CH_4 at room temperature, 0.5 mol L^{-1} H_2O_2 in deionized water, 70 mL total volume, 150 mg catalyst, 50 °C, 1000 rpm.

under isoconversion conditions, particularly for catalysts prepared by ion exchange or wetness impregnation. For example, for the two most active catalysts (Fig. 8), Cu-ZSM-5-30-IE and Cu-ZSM-5-30-WI, the selectivity to CH_3OOH (Fig. 11b) at $X_{OP} = 0.1\%$ is around 12% and 18%, respectively, whereas it is 30% for the ZSM-5-30 support. This pronounced loss of selectivity at relatively low conversions highlights the high activity of these catalysts not only for methane activation but also for CH_3OOH conversion. As the reaction progresses to $X_{OP} = 0.35\%$ (Fig. 11b), the selectivity further decreases slightly to around 7% for both Cu-ZSM-5–30 catalysts, indicating that the reaction rates at this point are very low compared to those of catalyst series with different SiO_2/Al_2O_3 ratios of 30, where the reaction rates are faster up to $X_{OP} = 0.1\%$ (Fig. 11a, S15a, and S15b). This is confirmed by the larger changes in selectivity observed in that conversion range.

The evolution of methanol selectivity as a function of the CH_4 conversion (Fig. 12, Fig. S16) shows, similarly to CH_3OOH (Fig. 11), that the product distribution is strongly governed by the interplay between Cu speciation and acidity, with Cu-modified catalysts systematically promoting overoxidation pathways rather than stabilizing CH_3OH as a primary product. At isoconversion conditions, all Cu-ZSM-5 catalysts exhibit higher methanol selectivity than the parent zeolite, which confirms the key role of Cu in the DOMTM to yield methanol as the target product; however, this selectivity rapidly vanishes as conversion increases, indicating that Cu species simultaneously promote methanol formation and strongly accelerate its subsequent oxidation to other products such as formaldehyde, formic acid, or CO_2. Among the ZSM-5-23 catalysts (Fig. 12a), Cu-ZSM-5-23-IE clearly achieved the highest selectivity, ranging between 100 and 59% in a CH_4 conversion range below 0.12%. Regarding the ZSM-5-30 catalysts (Fig. 12b), selectivities between 56–18% and 54–24% were observed for Cu-ZSM-5–30-WI and Cu-ZSM-5-30-IE, respectively, whereas the maximum selectivity reached with the ZSM-5-30 support was around 20%.

Fig. 13 shows the selectivity to formic acid (HCOOH) as a function of CH_4 conversion to oxygenated products (X_{OP}) for Cu-modified and parent ZSM-5 catalysts with SiO_2/Al_2O_3 ratios of 23 (Fig. 13a) and 30 (Fig. 13b), evidencing the progressive over-oxidation of primary oxygenate compounds such as CH_3OOH (Fig. 11) and CH_3OH (Fig. 12). The corresponding results for higher SiO_2/Al_2O_3 ratios are presented in the Supporting Information (Fig. S17). In Fig. 13a, the parent zeolite (ZSM-5-23) exhibits a steep increase in HCOOH selectivity with increasing X_{OP}, reaching values above 60%, which indicates extensive over-oxidation under highly acidic conditions, as also reported previously in the literature [11]; Cu introduction moderates this trend, particularly for the IE sample, which shows lower selectivities at isoconversion conditions, demonstrating partial suppression of over-oxidation pathways. In Fig. 13b, all catalysts display higher X_{OP} values, and the systematic rise in HCOOH selectivity with conversion becomes clearer, confirming that once initial oxygenates are formed,

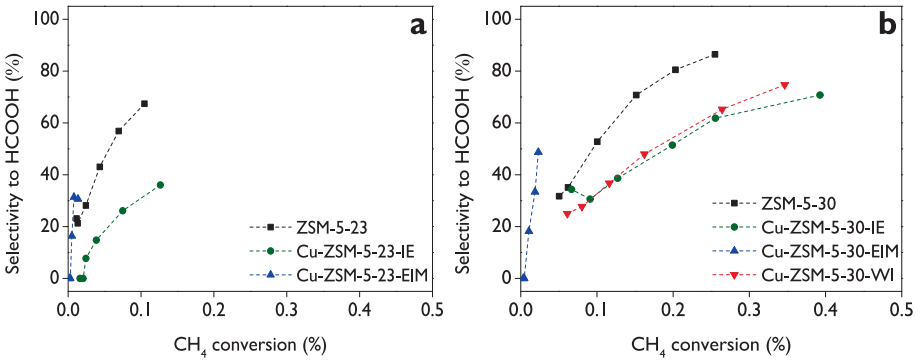

Fig. 13. Selectivity to formic acid (HCOOH) as a function of the CH_4 conversion to oxygenated products (X_{OP}) in the DOMTM route with H_2O_2 over catalysts based on **(a)** ZSM-5-23, and **(b)** ZSM-5-30. **Reaction conditions:** 30 bar CH_4 at room temperature, 0.5 mol L^{-1} H_2O_2 in deionized water, 70 mL total volume, 150 mg catalyst, 50 °C, 1000 rpm.

secondary oxidation dominates, as illustrated in Fig. 1a. Selectivity toward HCOOH of about 86% can be reached at 0.26% conversion with ZSM-5-30, followed by Cu-ZSM-5-30-WI (65%) and Cu-ZSM-5-30-IE (62%) at the same conversion level.

Overall, the monotonic increase in HCOOH selectivity with CH_4 conversion across all catalyst families indicates that formic acid is not a primary product of methane activation but instead arises from consecutive oxidation steps (Fig. 1a). Methane activation initially leads to methyl hydroperoxide (CH_3OOH) formation, which acts as the main intermediate. Depending on the catalyst composition, CH_3OOH undergoes further transformation either through rapid decomposition to CH_3OH followed by additional oxidation, or through direct overoxidation to HCOOH without significant methanol production, as in the observed case for the parent zeolites (Figs. S15-S17).

3.9. Methanol productivity over time

Across the ZSM-5 series, CH_3OH productivity is strongly governed by both the zeolite composition (different nominal SiO_2/Al_2O_3 ratio) and the Cu incorporation method. Only the most active catalysts for the CH_3OH production are discussed here, whereas samples with higher SiO_2/Al_2O_3 ratios are reported in Supporting Information (Fig. S18). For ZSM-5-23 (Fig. 14a), the parent material remains essentially inactive to activate methane and then produce methanol, with productivity below ~60 μmol g^{-1} after 4 h, whereas Cu-ZSM-5–23-IE shows a continuous and pronounced increase from 196 μmol g^{-1} at 15 min to 911 μmol g^{-1} at 4 h, with no clear plateau, indicating sustained methane activation. Cu-ZSM-5-23-EIM remains nearly inactive (<41 μmol g^{-1}) over the entire time range. At SiO_2/Al_2O_3 = 30 (Fig. 14b), Cu-modified catalysts prepared by IE and WI, outperform the parent ZSM-5-30, which plateaus at ~115 μmol g^{-1} after 4 h; Cu-ZSM-5-30-IE exhibits the highest productivity, rapidly reaching 620 μmol g^{-1} within 30 min and increasing to 1102 μmol g^{-1} at 4 h, whereas Cu-ZSM-5–30-WI shows fast initial formation (506 μmol g^{-1} at 30 min) followed by stabilization around 750–800 μmol g^{-1}, indicating progressive over-oxidation, as shown in Fig. 13, where formic acid is produced with all the catalysts. The EIM method, as previously discussed, resulted in a catalyst (Cu-ZSM-5-30-EIM) that weakly activates methane, reaching a productivity of <90 μmol g^{-1}. This behavior for EIM catalysts was already explained by the fact that the H_2O_2 decomposition pathway (Fig. S14) is favored over CH_4 activation and subsequent oxidation with these catalysts.

When methanol productivity is compared on a time-normalized basis (μmol $g^{-1}h^{-1}$), the performance of the Cu-ZSM-5 catalysts can be rigorously positioned relative to reported systems (Table S1). The highest activity in this work occurs at short reaction times (1 h), with Cu-ZSM-5-30-IE reaching a productivity of 750 μmol g^{-1} h^{-1} (Fig. 14b), reflecting efficient methane activation under oxidation with H_2O_2. This productivity surpasses most Cu- and Fe-based phthalocyanine catalysts supported on faujasite-type zeolites, such as $CuCl_{16}$Pc-Na-X (92 μmol g^{-1} h^{-1}), $CuCl_{16}$Pc-Na-Y (57 μmol g^{-1} h^{-1}), and $FeCl_{16}$Pc-Na-X (135 μmol g^{-1} h^{-1}), all of them operating at long reaction times [9]. Furthermore, Cu-ZSM-5–30-IE surpasses the productivity reported with Fe/silicalite-1 (560 μmol g^{-1} h^{-1}) [11] and Pd-Au/CNTs (278 μmol g^{-1} h^{-1}) [18], which are commonly cited as moderate-activity systems. Noble-metal zeolite catalysts exhibit slightly higher productivities, such as Au/ZSM-5 (1000 μmol g^{-1} h^{-1}) [16], Rh/ZSM-5 (1224 μmol g^{-1} h^{-1}) [19], and Au/H-MOR (1300 μmol g^{-1} h^{-1}) [17]. However, these systems operate typically at elevated temperatures (70–150 °C). Among the most active systems reported, such as Pd/ZSM-5 (5000 μmol g^{-1} h^{-1}) [16] and AuPd/ZSM-5 (91600 μmol g^{-1} h^{-1}) [16], substantially higher

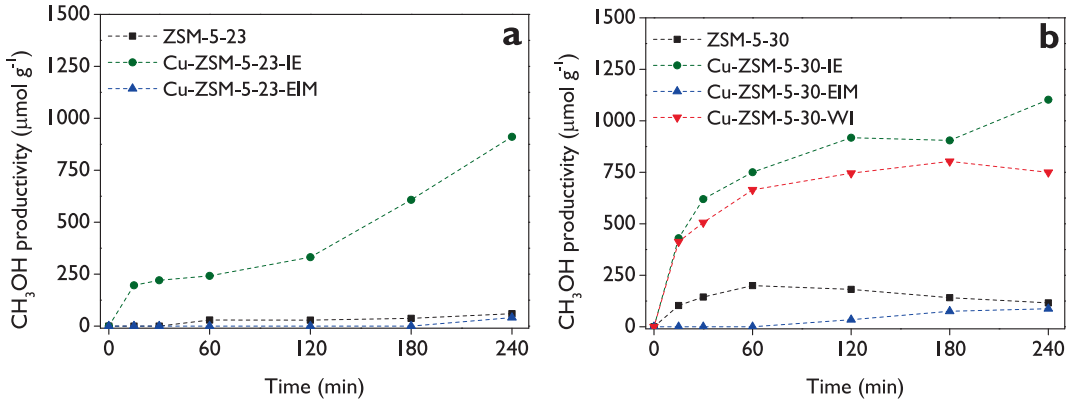

Fig. 14. Methanol productivity in the DOMTM route with H_2O_2 over catalysts based on **(a)** ZSM-5–23, and **(b)** ZSM-5-30. **Reaction conditions:** 30 bar CH_4 at room temperature, 0.5 mol L^{-1} H_2O_2 in deionized water, 70 mL total volume, 150 mg catalyst, 50 °C, 1000 rpm.

productivities are achieved under conditions involving in situ H_2O_2 formation. Importantly, the present study demonstrates that high methanol formation rates are obtained only when Cu dispersion is around 5%, Brønsted acid site density is intermediate (~0.5–0.7 μmol m^{-2}), and BAS/LAS ratios are balanced (≈1–1.7). Taken together, these results show that the Cu–ZSM-5 catalysts developed here exhibit initial methanol formation rates comparable to those reported in the literature for H_2O_2-mediated systems (Table S1), while providing mechanistic insight into the metal–acid synergy driving the reaction.

3.10. Formation of formaldehyde and CO_2

CO_2 is typically overlooked in the literature on direct oxidation of methane to methanol, which significantly affects the reported product distribution [21]. Here, the production of formaldehyde and CO_2 in the batch reactor was analyzed, as discussed in the Materials and Methods section, only after 4h of reaction, as shown in Fig. 15 for the most active catalysts, and Fig. S19 for the other materials. Therefore, the selectivity to all liquid-phase products is reported at 4 h under the tested conditions, and the total methane conversion can thus be calculated, as specified in Eq. (6). This total conversion is higher than the conversion to oxygenated products (X_{OP}) reported in all previous sections. Fig. 15

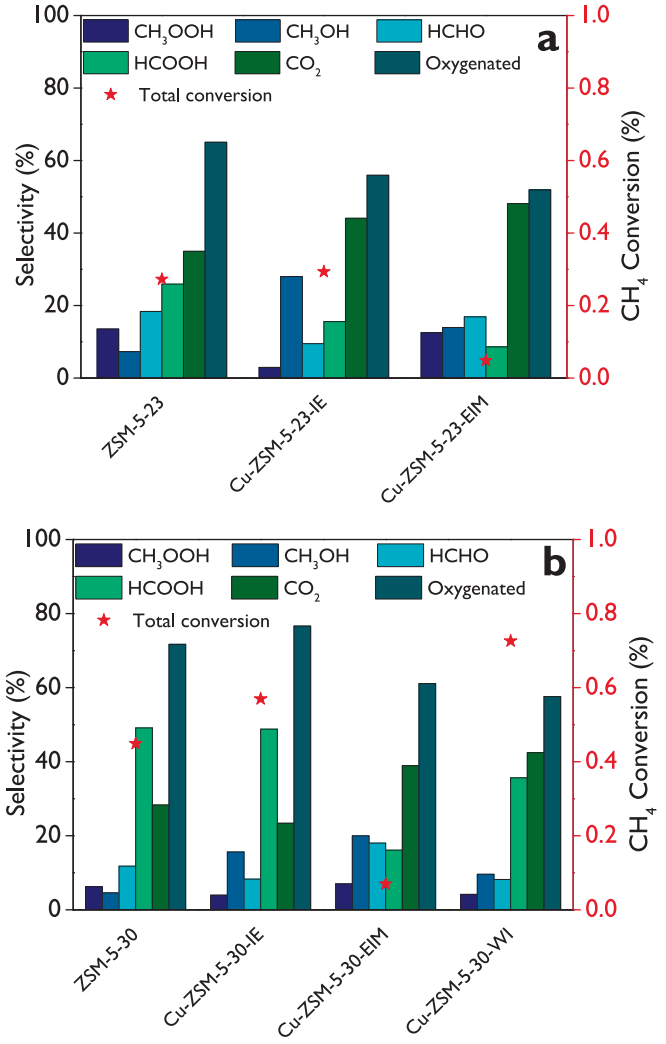

Fig. 15. Selectivity in the liquid phase of all products (oxygenated and CO_2) and total methane conversion (X_T) after 4 h in the DOMTM route with H_2O_2 over catalysts based on **(a)** ZSM-5–23, and **(b)** ZSM-5-30. **Reaction conditions:** 30 bar CH_4 at room temperature, 0.5 mol L^{-1} H_2O_2 in deionized water, 70 mL total volume, 150 mg catalyst, 50 °C, 1000 rpm.

and Fig. S19 show that selectivity is critically governed by zeolite acidity and the Cu incorporation method. Across all SiO_2/Al_2O_3 ratios, the EIM method yielded catalysts with poor total conversions, below 0.07%. Regarding the other catalysts, Fig. 15a shows that the total CH_4 conversion (X_T) remains moderate (≈0.25–0.30%), while CO_2 selectivity is considerably high, with values between 35 and 48%, the remainder corresponding to oxygenated products (CH_3OOH + CH_3OH + HCHO + HCOOH). HCHO represented roughly 10–20% of the liquid products after 4 h, indicating that high acidity favors rapid over-oxidation, even when primary oxygenates such as CH_3OOH and CH_3OH are formed.

In Fig. 15b, the most balanced behavior is observed, with total conversion increasing to ≈0.45–0.73% (compared to X_{OP} = 0.39% for Cu-ZSM-5–30-IE, Fig. 10b), while oxygenated selectivities reached 77%, 71%, and 58% for Cu-ZSM-5–30-IE, ZSM-5-30, and Cu-ZSM-5-30-WI, respectively. CO_2 formation is minimized to 23% with the ion-exchange catalyst, while HCHO selectivity is also minimized with this catalyst, with a value of 8.2%, equal to that of Cu-ZSM-5–30-WI.

Figs. S19a and S19b illustrate that the parent zeolites (ZSM-5-50 and ZSM-5-80) surpass the total conversion of the Cu-ZSM-5 catalysts, showing trends similar to those observed in Figs. S13a and 13b. This was attributed to the higher BAS/LAS ratios (2.0–2.2) of the parent zeolites compared to the Cu-modified counterparts (BAS/LAS < 1.0). These results show that only the presence of Cu is not sufficient to effectively catalyze the reaction; rather, an appropriate balance of Brønsted and Lewis acid sites is required. Additionally, CO_2 selectivity with these materials ranges between 31% and 41%. Interestingly, catalysts synthesized by ion-exchange produced the lowest CO_2 selectivities among all tested catalysts, with values of 11% (Cu-ZSM-5-80-IE) and 18% (Cu-ZSM-5-50-IE); however, total CH_4 conversions with these materials are very poor, below <0.23%.

3.11. A summary: Optimal windows for key descriptors in DOMTM

The importance of the BAS/LAS ratio, Brønsted acid site density, and isolated Cu^{2+} species has been explained throughout the text. Similar to the dependencies of TOF on different parameters (Fig. 8, Fig. S12), Fig. 16 and Fig. S20 present several correlations for all the catalysts evaluated in this work, clearly showing that Cu-ZSM-5-30-IE/WI are the most efficient catalysts for methanol production.

Fig. 16a demonstrates that the highest CH_4 conversion at 4 h is achieved with the Cu-ZSM-5–30-IE catalyst, which exhibited the highest Cu dispersion (4.6%). In addition, the highest CH_4 conversions (Fig. 16c, Fig. S20a) are obtained with materials exhibiting BAS/LAS ratios in the range of 1.2–2.2 (Cu-ZSM-5-30-WI > Cu-ZSM-5–30-IE > ZSM-5–80 > ZSM-5–50), with the highest value of 0.73% for Cu-ZSM-5–30-WI. Notably, materials with BAS/LAS values outside this range exhibit conversions below 0.3%. Similarly, Fig. 16e and Fig. S20c show that the two highest CH_4 conversions are obtained for Brønsted acid site densities of 0.57 and 0.58 μmol m^{-2}, corresponding to Cu-ZSM-5–30-WI and Cu-ZSM-5–30-IE, respectively.

Fig. 16b shows that CH_3OH productivity at 4 h increases sharply with Cu dispersion only beyond ~1–2% dispersion, reaching maxima of 1102 μmol g^{-1} for ion-exchanged samples with Cu dispersion around ~4–5%, whereas samples below ~1% dispersion display activity lower than 250 μmol g^{-1}, demonstrating that poorly dispersed Cu is largely inactive. Fig. 16d and Fig. S20b reveal a clear optimum in the BAS/LAS ratio centered at BAS/LAS ≈ 1–1.7, and that the productivity drops steeply at lower ratios (<0.5), where values remain below 250 μmol g^{-1}, and also at high ratios (>3–5), where methanol formation collapses, confirming that both acid imbalance extremes are detrimental, and conversely, that methane oxidation is maximized only at an intermediate acid balance. Fig. 16f and Fig. S20d quantify this effect in terms of Brønsted acid site density, showing a pronounced maximum (749–1102 μmol g^{-1}) at intermediate BAS densities of ~0.5–0.7 μmol m^{-2}, while lower densities (<0.3 μmol m^{-2}) and higher densities (>0.9–1.1 μmol m^{-2}) yield productivities typically below 300 μmol g^{-1}. Similar trends were observed

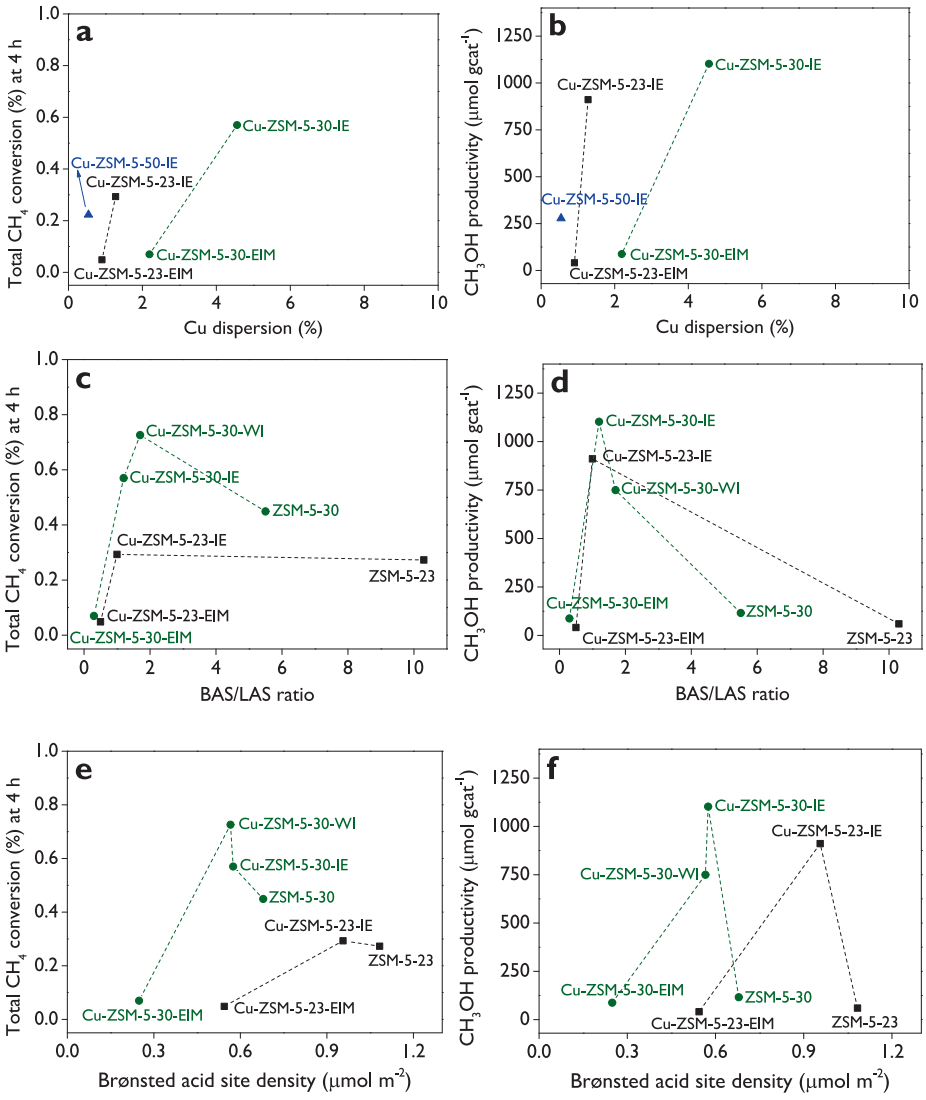

Fig. 16. Dependence of the total CH_4 conversion at 4 h **(a, c, e)** and CH_3OH productivity at 4 h **(b, d, f)** with Cu dispersion **(a, b)**, BAS/LAS molar ratio **(c, d)**, and Brønsted acid site density **(e, f)**. **Reaction conditions:** 30 bar CH_4 at room temperature, 0.5 mol L^{-1} H_2O_2 in deionized water, 70 mL total volume, 150 mg catalyst, 50 °C, 1000 rpm.

when productivity is reported per mass of copper (Fig. S21). These results indicate that maximum CH_3OH productivity is achieved only when well-dispersed Cu sites coexist with an adequately balanced acidity, which is obtained at an intermediate SiO_2/Al_2O_3 ratio of 30.

The observed relationships support the existence of a synergistic effect between Brønsted acid sites (Al–OH–Si) and Lewis acid sites associated with isolated Cu^{2+} species. As demonstrated, catalysts containing mainly Brønsted acid sites (BAS/LAS > 10) or only Lewis acid sites (BAS/LAS → 0) show negligible methanol productivity (Fig. 16d and Fig. S20b), confirming that neither type of site alone is sufficient for effective synthesis of methanol. The activity in the direct oxidation of methane can thus be attributed to the presence of effective BAS–LAS pairs, where Brønsted sites from the zeolite framework operate in proximity to Lewis sites from isolated Cu^{2+}, enabling methane activation, controlled reaction with H_2O_2, and selective CH_3OH formation.

The existence of an optimal SiO_2/Al_2O_3 ratio (~30) for BAS-LAS cooperativity can be rationalized not only in terms of acid site concentration but also through the geometric proximity between Cu^{2+} species and neighboring Brønsted acid sites. Cu^{2+} exchange at 2Z sites requires two nearby framework Al atoms, meaning that the probability of forming such sites decreases as the Si/Al ratio increases due to Al distribution constraints. At the same time, each Cu^{2+} replaces two H^+, reducing the number of Brønsted acid sites and the formation of Lewis acid sites. Effective BAS-LAS cooperativity, therefore, depends on a balance: sufficient Al pairs to host Cu^{2+} (favoring low Si/Al), while retaining enough nearby, unexchanged H^+ sites (favoring higher Si/Al).

At $SiO_2/Al_2O_3 = 23$, the high Al density promotes Cu^{2+} exchange, but also leads to excessive consumption of Brønsted sites, disrupting the BAS/LAS balance. At higher ratios (50–80), Al pairs become too scarce, limiting Cu^{2+} incorporation and reducing overall Brønsted acidity below the required range. In contrast, $SiO_2/Al_2O_3 = 30$ provides a suitable support where both sufficient Cu^{2+} sites and neighboring H^+ sites coexist. Thus, the observed optimum likely reflects a balance between site proximity and site density, rather than a simple dependence on total acid concentration.

3.12. Reaction pathway

The nature of the active centers for methane to methanol conversion over Cu-supported zeolites has been more clearly established for gas-phase reactions than for liquid-phase. In particular, seminal work by Groothaert and co-workers [61–63] demonstrated that mono(μ-oxo) dicopper and bis(μ-oxo) dicopper complexes are the active sites for high-temperature, gas-phase methane oxidation. It should be noted, however,

that these studies employ a stepwise stoichiometric protocol involving sequential high-temperature catalyst activation (300–450 °C) in O_2 or N_2O, methane reaction, and methanol extraction, in which the active Cu-oxo site is consumed per cycle rather than continuously regenerated. This is fundamentally different from the liquid-phase catalytic conditions employed in the present work, in which H_2O_2 serves as a continuously available oxidant at 50 °C. In contrast, the identity of the active centers in the liquid-phase direct oxidation of methane to methanol (DOMTM) remains unresolved. This ambiguity arises from the structural complexity of Cu/zeolite systems, where different Cu species can be formed depending on the zeolite framework, the Cu introduction method, and post-synthesis thermal treatments [4]. A variety of Cu species have been identified using spectroscopic techniques, such as mononuclear Cu^{+}, Cu^{2+}, and $[CuOH]^{+}$ species [4,64]. On this basis, Kulkarni et al. [65] proposed $[Cu^{II}OH]^{+}$ species located in 8-membered ring zeolites as the active sites, although this conclusion relied exclusively on DFT calculations. More recently, Sogukkanli et al. [66] suggested isolated Cu species as the active centers for the CO-assisted DOMTM route, while Gabrienko et al. [67] proposed that Cu^{2+} cations associated with framework Al-O-Si sites may exist as either isolated or paired species. Similarly, Meyet et al. [68] reported well-dispersed monomeric Cu^{II} species supported on alumina as active centers, although in a stepwise reaction sequence involving catalyst activation, methane reaction, and methanol extraction. Overall, despite significant progress, the identification of the true active sites under liquid-phase DOMTM conditions remains an open question.

In this work, based on the characterization of the most active catalyst (Cu-ZSM-5-30-IE), isolated Cu^{2+} species (Fig. 6b and Fig. 7), acting as Lewis acid sites in proximity to framework Brønsted acid sites, are proposed to form BAS–LAS pairs responsible for methane oxidation in the liquid phase. Accordingly, a confined radical-mediated reaction pathway is proposed (Fig. 17). In Step A, H_2O_2 is activated at the Brønsted acid site (Al-OH-Si), leading to reactive oxygen species, specifically hydroxyl radicals (•OH) and hydroperoxyl radicals (•OOH), consistent with previous reports on the role of radical chemistry in the kinetics of methane oxidation [4,69,70]. In Step B, CH_4 is activated within the neighboring BAS-LAS environment through hydrogen abstraction by •OH at the Cu^{2+} Lewis acid site, forming methyl radicals $•CH_3$ and water. The methyl radicals rapidly react with •OOH to produce methyl hydroperoxide (step C). This adsorbed intermediate gives place, within the zeolite channels, to radicals $CH_3O•$ and •OH, and then, hydrogen transfer yields methanol, which is released into the liquid phase, regenerating the BAS-LAS active pair for another cycle (step D).

In the parent ZSM-5 materials, which do not contain added Lewis acid sites, methane activation is proposed to occur via hydrogen abstraction by hydroxyl radicals generated from the homolytic cleavage of H_2O_2 at Brønsted acid sites within the confined channels [71,72]. The observed conversion is facilitated by the confinement and the density of acid sites, which stabilize radical intermediates sufficiently to allow partial oxidation, even in the absence of metal sites, although the lack of metal centers results in lower methanol selectivity compared to Cu-ZSM-5-30. Under H_2O_2-rich conditions, methanol undergoes consecutive oxidation (step E) to formaldehyde, formic acid, and CO_2, accounting for the observed over-oxidation pathways and the associated selectivity losses at longer reaction times.

4. Conclusions

This work systematically investigated the direct oxidation of methane to methanol over Cu-ZSM-5 catalysts as a model system, using H_2O_2 as the oxidant under mild conditions (water as solvent, 50 °C), to establish robust structure–activity relationships that go beyond the isolated or qualitative correlations commonly reported in the literature. The roles of copper speciation and dispersion, total acidity, the balance between Brønsted and Lewis acid sites, the synergistic interaction of BAS-LAS pairs, and the framework aluminum environment were explored in a unified manner. The preservation of the zeolitic MFI framework in all prepared catalysts was confirmed by XRD and SEM. The concentration of Lewis and Brønsted acid sites was determined from pyridine-FTIR analyses. Copper dispersion was successfully evaluated using a combined N_2O oxidation-H_2-TPR approach, which yielded the most reliable estimate of accessible copper sites. UV–Vis-DRS and H_2-TPR analyses consistently indicated that isolated Cu^{2+} species dominate under the studied conditions and are responsible for methanol formation along with the Brønsted acid sites (Al-OH-Si), supporting the plausible reaction pathway proposed.

Methanol formation exhibited a maximum in TOF within a narrow window of Brønsted acid site density (0.58–0.96 μmol m^{-2}), corresponding to BAS/LAS molar ratios between approximately 1.0 and 1.7, depending on the framework aluminium content. The highest values

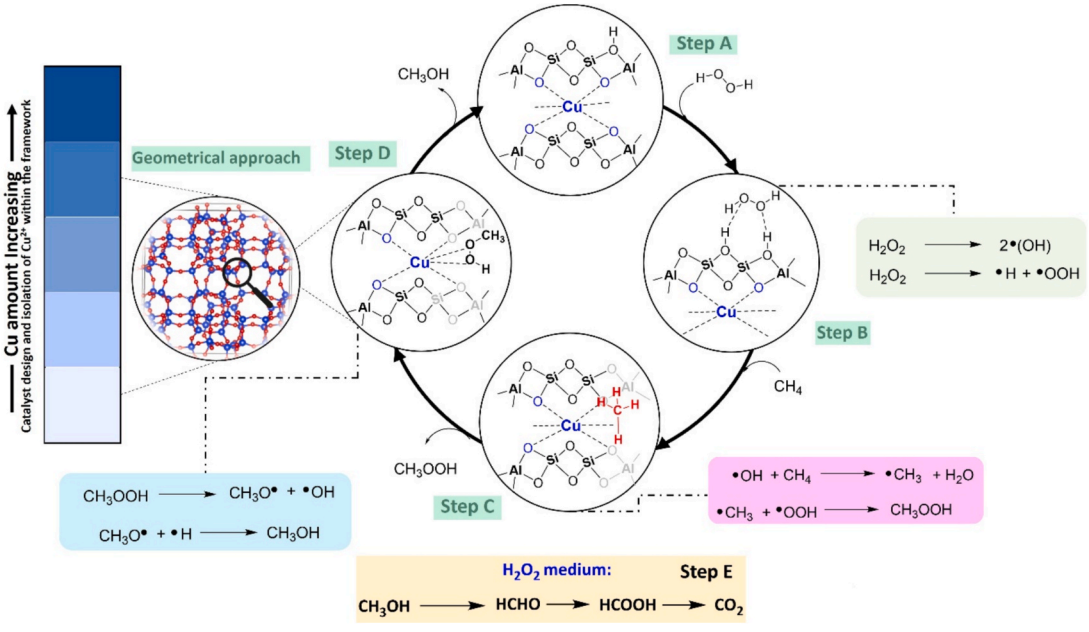

Fig. 17. Plausible reaction pathway for the direct oxidation of methane to methanol over Cu-ZSM-5-30-IE using H_2O_2 as an oxidant and water as the solvent.

were observed for Cu-ZSM-5-30 catalysts with BAS/LAS = 1.2 (IE) and 1.7 (WI), and for Cu-ZSM-5-23-IE with BAS/LAS = 1.0, whereas catalysts outside this combined acidity-density window exhibited negligible activity. Importantly, several ZSM-5-50 and ZSM-5-80 materials displayed BAS/LAS ratios within this range but failed to produce methanol due to insufficient Brønsted acid site densities, demonstrating that BAS/LAS alone is not a reliable predictor of catalytic performance unless the acid site density and Cu species are simultaneously considered.

Copper dispersion positively influences TOF_D, but high dispersion alone does not guarantee high activity when acidity is suboptimal. The most active catalyst, Cu-ZSM-5-30-IE, combines the highest measurable Cu dispersion with Brønsted acidity within the identified optimal range, emphasizing the cooperative role of metal dispersion, acid functionality, and the synergistic interaction of BAS-LAS pairs. Moreover, a linear correlation between TOF_D and BAS/LAS was observed, largely independent of the nominal SiO_2/Al_2O_3 ratio.

In this work, several contributions were made toward a more quantitative understanding of the direct oxidation of methane to methanol (DOMTM) over Cu-ZSM-5 catalysts: **i)** it is shown that the Al_{VI}/Al_{IV} ratio and the BAS/LAS molar ratio are not uniquely correlated in Cu-exchanged ZSM-5, indicating that copper incorporation and framework aluminum coordination modify acidity descriptors; **ii)** copper dispersion is quantified using a combined N_2O oxidation and H_2-TPR approach, providing a more reliable estimate of accessible copper sites than methods based on TEM and TPR alone; **iii)** turnover frequencies normalized by total acidity and copper dispersion are correlated with key physicochemical properties, such as Cu dispersion, BAS/LAS ratio, and Brønsted acid site density, revealing non monotonic structure–activity relationships; **iv)** characteristic ranges of BAS/LAS ratios and Brønsted acid site densities are identified as typical conditions for enhanced methanol productivity; **v)** based on the observed catalytic trends and copper speciation characterization, a plausible reaction pathway is proposed in which isolated Cu^{2+} species act as the active centers for methane activation, facilitated by the synergistic BAS-LAS pairs; and **vi)** rigorous quantification of all oxidation products is performed, including dissolved CO_2 at conversions often below 1%.

Overall, this work establishes that high methanol productivity of 750 μmol g^{-1} h^{-1}, with a selectivity of 49%, in the DOMTM route over Cu-ZSM-5 catalysts using H_2O_2 as an oxidant arises from a specific balance between copper dispersion, Brønsted acid site density, the synergistic interaction of BAS-LAS pairs, and the framework aluminum environment, rather than from any single descriptor. The structure–activity relationships identified here provide a benchmark for evaluating zeolitic catalysts and underscore the necessity of comprehensive characterization and product analysis in low-conversion methane oxidation studies. Finally, although H_2O_2 is not economically practical as an oxidant at an industrial scale, because its cost currently exceeds the value of methanol, it remains an essential mechanistic probe for elucidating structure–activity relationships under mild conditions.

CRediT authorship contribution statement

Luis A. Gallego-Villada: Writing – original draft, Methodology, Investigation, Formal analysis, Conceptualization. **Päivi Mäki-Arvela:** Writing – review & editing, Supervision, Resources, Funding acquisition, Conceptualization. **Kari Eränen:** Methodology, Conceptualization. **Pasi Virtanen:** Conceptualization. **Narendra Kumar:** Conceptualization. **Mika Lastusaari:** Investigation. **Dmitry Yu. Murzin:** Writing – review & editing, Supervision, Resources, Funding acquisition, Conceptualization.

Declaration of competing interest

The authors declare that they have no known competing financial interests or personal relationships that could have appeared to influence the work reported in this paper.

Acknowledgments

The authors acknowledge the Research Council of Finland for funding through the project "Methane to methanol by biomimetic catalysts" (Project No. 361444). The authors also thank the Institute of Biomedicine, University of Turku, which receives financial support from Biocenter Finland, for the analysis of samples by transmission electron microscopy (TEM). The authors would like to express their gratitude to Dr. Julián Sánchez-Velandia for his valuable advice on the reaction pathway.

Appendix A. Supplementary material

The Supporting Information includes a summary of recent heterogeneous catalytic systems for the direct oxidation of methane to methanol in liquid phase; details of the quantification of liquid-phase products by HPLC and ^1H NMR; quantification of dissolved CO_2 via potentiometric titration; XRD patterns of spent catalysts; determination of copper leaching by XRF and ICP-OES; SEM-EDX analysis of fresh catalysts; comparison of the textural properties of the fresh catalysts using three methods; pore size distributions using NL-DFT method for the fresh catalysts; N_2 adsorption–desorption isotherms and pore size distributions for spent catalysts; quantification of acidity through pyridine-FTIR; ^{29}Si MAS NMR of selected catalysts; TEM images; limitations of TEM as a technique for measuring Cu dispersion; TOF as a function of the BAS/LAS ratio, Brønsted acid site density, and Al_{VI}/Al_{IV} ratio; methane conversion as a function of time for catalysts based on SiO_2/Al_2O_3 = 50 and 80; H_2O_2 conversion profiles; selectivity to CH_3OOH, CH_3OH, and HCOOH as a function of the methane conversion for catalysts based on SiO_2/Al_2O_3 = 50 and 80; methanol productivity as a function of time for catalysts based on SiO_2/Al_2O_3 = 50 and 80; quantification of formaldehyde and CO_2 for catalysts based on SiO_2/Al_2O_3 = 50 and 80; correlations of catalytic performance with catalyst physicochemical parameters.

Supplementary data to this article can be found online at https://doi.org/10.1016/j.jcat.2026.116924.

Data availability

Data will be made available on request.

References

[1] A. Caballero, P.J. Pérez, Methane as raw material in synthetic chemistry: the final frontier, Chem. Soc. Rev. 42 (2013) 8809, https://doi.org/10.1039/c3cs60120j.
[2] L. Sun, Y. Wang, N. Guan, L. Li, Methane activation and utilization: current status and future challenges, Energ. Technol. 8 (2020), https://doi.org/10.1002/ente.201900826.
[3] C.A. Haynes, R. Gonzalez, Rethinking biological activation of methane and conversion to liquid fuels, Nat. Chem. Biol. 10 (2014) 331–339, https://doi.org/10.1038/nchembio.1509.
[4] N.F. Dummer, D.J. Willock, Q. He, M.J. Howard, R.J. Lewis, G. Qi, S.H. Taylor, J. Xu, D. Bethell, C.J. Kiely, G.J. Hutchings, Methane oxidation to methanol, Chem. Rev. 123 (2023) 6359–6411, https://doi.org/10.1021/acs.chemrev.2c00439.
[5] W. Taifan, J. Baltrusaitis, CH_4 conversion to value added products: potential, limitations and extensions of a single step heterogeneous catalysis, Appl Catal B 198 (2016) 525–547, https://doi.org/10.1016/j.apcatb.2016.05.081.
[6] G. Qi, T.E. Davies, A. Nasrallah, M.A. Sainna, A.G.R. Howe, R.J. Lewis, M. Quesne, C.R.A. Catlow, D.J. Willock, Q. He, D. Bethell, M.J. Howard, B.A. Murrer, B. Harrison, C.J. Kiely, X. Zhao, F. Deng, J. Xu, G.J. Hutchings, Au-ZSM-5 catalyses the selective oxidation of CH_4 to CH_3OH and CH_3COOH using O_2, Nat. Catal. 5 (2022) 45–54, https://doi.org/10.1038/s41929-021-00725-8.
[7] J. Tian, J. Tan, Z. Zhang, P. Han, M. Yin, S. Wan, J. Lin, S. Wang, Y. Wang, Direct conversion of methane to formaldehyde and CO on B_2O_3 catalysts, Nat. Commun. 11 (2020) 5693, https://doi.org/10.1038/s41467-020-19517-y.
[8] T. Yu, Z. Li, L. Lin, S. Chu, Y. Su, W. Song, A. Wang, B.M. Weckhuysen, W. Luo, Highly selective oxidation of methane into methanol over Cu-promoted monomeric Fe/ZSM-5, ACS Catal. 11 (2021) 6684–6691, https://doi.org/10.1021/acscatal.1c00905.
[9] R. Raja, P. Ratnasamy, Direct conversion of methane to methanol, Appl. Catal. A. Gen. 158 (1997) L7–L15, https://doi.org/10.1016/S0926-860X(97)00105-1.
[10] M.M. Forde, B.C. Grazia, R. Armstrong, R.L. Jenkins, M.H.A. Rahim, A.F. Carley, N. Dimitratos, J.A. Lopez-Sanchez, S.H. Taylor, N.B. McKeown, G.J. Hutchings,

Methane oxidation using silica-supported N-bridged di-iron phthalocyanine catalyst, J. Catal. 290 (2012) 177–185, https://doi.org/10.1016/j.jcat.2012.03.013.
[11] C. Hammond, M.M. Forde, M.H. Ab Rahim, A. Thetford, Q. He, R.L. Jenkins, N. Dimitratos, J.A. Lopez-Sanchez, N.F. Dummer, D.M. Murphy, A.F. Carley, S. H. Taylor, D.J. Willock, E.E. Stangland, J. Kang, H. Hagen, C.J. Kiely, G. J. Hutchings, Direct catalytic conversion of methane to methanol in an aqueous medium by using copper-promoted Fe-ZSM-5, Angew. Chem. Int. Ed. 124 (2012) 5219–5223, https://doi.org/10.1002/ange.201108706.
[12] B. Yu, L. Cheng, S. Dai, Y. Jiang, B. Yang, H. Li, Y. Zhao, J. Xu, Y. Zhang, C. Pan, X. Cao, Y. Zhu, Y. Lou, Silver and copper dual single atoms boosting direct oxidation of methane to methanol via synergistic catalysis, Adv. Sci. 10 (2023), https://doi.org/10.1002/advs.202302143.
[13] S. An, S. Zhao, J. Jin, T. He, Y. Wang, N. Kong, J. Zhou, W. Li, Direct oxidation of methane to methanol over copper and zinc synergistic co-modified H-ZSM-5 catalyst, Mol. Catal. 574 (2025) 114863, https://doi.org/10.1016/j.mcat.2025.114863.
[14] X. Tang, L. Wang, B. Yang, C. Fei, T. Yao, W. Liu, Y. Lou, Q. Dai, Y. Cai, X.M. Cao, W. Zhan, Y. Guo, X.Q. Gong, Y. Guo, Direct oxidation of methane to oxygenates on supported single Cu atom catalyst, Appl. Catal. B 285 (2021), https://doi.org/10.1016/j.apcatb.2020.119827.
[15] C.-C. Liu, C.-Y. Mou, S.-S.-F. Yu, S.I. Chan, Heterogeneous formulation of the tricopper complex for efficient catalytic conversion of methane into methanol at ambient temperature and pressure, Energy Environ. Sci. 9 (2016) 1361–1374, https://doi.org/10.1039/C5EE03372A.
[16] Z. Jin, L. Wang, E. Zuidema, K. Mondal, M. Zhang, J. Zhang, C. Wang, X. Meng, H. Yang, C. Mesters, F.-S. Xiao, Hydrophobic zeolite modification for in situ peroxide formation in methane oxidation to methanol, Science 367 (2020) (1979) 193–197, https://doi.org/10.1126/science.aaw1108.
[17] W. Wang, W. Zhou, Y. Tang, W. Cao, S.R. Docherty, F. Wu, K. Cheng, Q. Zhang, C. Copéret, Y. Wang, Selective oxidation of methane to methanol over Au/H-MOR, J. Am. Chem. Soc. 145 (2023) 12928–12934, https://doi.org/10.1021/jacs.3c04260.
[18] Y. He, C. Luan, Y. Fang, X. Feng, X. Peng, G. Yang, N. Tsubaki, Low-temperature direct conversion of methane to methanol over carbon materials supported Pd-Au nanoparticles, Catal. Today 339 (2020) 48–53, https://doi.org/10.1016/j.cattod.2019.02.043.
[19] J. Shan, M. Li, L.F. Allard, S. Lee, M. Flytzani-Stephanopoulos, Mild oxidation of methane to methanol or acetic acid on supported isolated rhodium catalysts, Nature 551 (2017) 605–608, https://doi.org/10.1038/nature24640.
[20] M. Chauhan, B. Rana, P. Gupta, R. Kalita, C. Thadhani, K. Manna, Tailored pore-confined single-site iron(III) catalyst for selective CH_4 oxidation to CH_3OH or CH_3CO_2H using O_2, Nat. Commun. 15 (2024) 9798, https://doi.org/10.1038/s41467-024-54101-8.
[21] A. Oda, K. Ichino, Y. Yamamoto, T. Ohtsu, W. Shi, Y. Sawada, J. Kumagai, K. Sawabe, A. Satsuma, Hydrophobic, acid-free zeolite-confined Pt–Cu nanoalloys break activity–selectivity limits in low-temperature methane-to-methanol oxidation, J. Am. Chem. Soc. 147 (2025) 30009–30021, https://doi.org/10.1021/jacs.5c07414.
[22] Structure Commission of the International Zeolite Association, Database of Zeolite Structures, (2017). http://www.iza-structure.org/databases/ (accessed December 4, 2025).
[23] L.A. Gallego-Villada, J.T. García-Sánchez, G. Lauer, P. Mäki-Arvela, J.E. Sánchez-Velandia, D.Y. Murzin, Physicochemical characterization of solid catalysts: morphological, structural, textural, reducibility, and acid-base insights, ChemCatChem (2025), https://doi.org/10.1002/cctc.202500974.
[24] C. Boruban, E. Nalbant Esenturk, Synthesis of CuO nanostructures on zeolite-Y and investigation of their CO_2 adsorption properties, J. Mater. Res. 32 (2017) 3669–3678, https://doi.org/10.1557/jmr.2017.337.
[25] A. Bayout, C. Cammarano, I.M. Costa, G. Veryasov, T. Mineva, A. Galarneau, V. Hulea, Effect of acidity and crystal morphology of ZSM-5 in toluene alkylation with methyl mercaptan, ChemCatChem 17 (2025), https://doi.org/10.1002/cctc.202501016.
[26] L.A. Gallego-Villada, J.M. Cueto, P. del M. Alonso-Doncel, E.A. Mäki-Arvela, D. P. Alarcón, D. Serrano, Y. Murzin, Dendritic ZSM-5 zeolites as highly active catalysts for the valorization of monoterpene epoxides, Green Chem. 26 (2024) 10512–10528, https://doi.org/10.1039/D4GC04003A.
[27] S.V. Quintana-Arturo, L.A. Gallego-Villada, E.A. Alarcón, D.Y. Murzin, One-Pot Transformation of R-(+)-Limonene over Sr- and Sn-Modified hierarchical Y zeolite catalysts: toward sustainable conversion routes, ACS Sustain. Chem. Eng. (2025), https://doi.org/10.1021/acssuschemeng.5c08939.
[28] R. Barakov, N. Shcherban, P. Mäki-Arvela, P. Yaremov, I. Bezverkhyy, J. Wärnå, D. Y. Murzin, Hierarchical beta zeolites As catalysts in α-pinene oxide isomerization, ACS Sustain. Chem. Eng. 10 (2022) 6642–6656, https://doi.org/10.1021/acssuschemeng.2c00441.
[29] L. Briones, A. Cordero, M. Alonso-Doncel, D.P. Serrano, J.M. Escola, Catalytic upgrading of a model polyethylene pyrolysis oil by hydroconversion over Ni-containing hierarchical Beta zeolites with tailored acidity, Appl. Catal. B 341 (2024) 123359, https://doi.org/10.1016/j.apcatb.2023.123359.
[30] S. Shimizu, N. Matubayasi, Surface area estimation: replacing the brunauer–emmett–teller model with the statistical thermodynamic fluctuation theory, Langmuir 38 (2022) 7989–8002, https://doi.org/10.1021/acs.langmuir.2c00753.
[31] M. Senila, O. Cadar, Modification of natural zeolites and their applications for heavy metal removal from polluted environments: challenges, recent advances, and perspectives, Heliyon 10 (2024) e25303, https://doi.org/10.1016/j.heliyon.2024.e25303.
[32] O. Ojelabi, S. Yousatit, U. Rashid, C. Ngamcharussrivichai, Mild dealumination of H-ZSM-5 zeolite for enhanced conversion of glucose into 5-hydroxymethylfurfural in a biphasic solvent system, Catalysts 13 (2023) 982, https://doi.org/10.3390/catal13060982.
[33] T. Kurniawan Saepurahman, M.A. Azis Jayanudin, Simultaneous impregnation-dealumination to produce SnO_2-hierarchical zeolite for methylene blue elimination via adsorption-photodegradation, Case Stud. Chem. Environ. Eng. 9 (2024) 100613, https://doi.org/10.1016/j.cscee.2024.100613.
[34] V.L. Sushkevich, J.A. van Bokhoven, Effect of Brønsted acid sites on the direct conversion of methane into methanol over copper-exchanged mordenite, Catal. Sci. Technol. 8 (2018) 4141–4150, https://doi.org/10.1039/C8CY01055B.
[35] G. Paul, C. Bisio, I. Braschi, M. Cossi, G. Gatti, E. Gianotti, L. Marchese, Combined solid-state NMR, FT-IR and computational studies on layered and porous materials, Chem. Soc. Rev. 47 (2018) 5684–5739, https://doi.org/10.1039/C7CS00358G.
[36] M. Jin, M. Ravi, C. Lei, C.J. Heard, F. Brivio, Z. Tošner, L. Grajciar, J.A. van Bokhoven, P. Nachtigall, Dynamical equilibrium between brønsted and lewis sites in zeolites: framework-associated octahedral aluminum, Angew. Chem. Int. Ed. 62 (2023), https://doi.org/10.1002/anie.202306183.
[37] K. Chen, Z. Gan, S. Horstmeier, J.L. White, Distribution of aluminum species in zeolite catalysts: ^{27} Al NMR of framework, partially-coordinated framework, and non-framework moieties, J. Am. Chem. Soc. 143 (2021) 6669–6680, https://doi.org/10.1021/jacs.1c02361.
[38] F. Deng, Y. Yue, C. Ye, Observation of nonframework Al species in zeolite β by solid-state NMR spectroscopy, J. Phys. Chem. B 102 (1998) 5252–5256, https://doi.org/10.1021/jp9801929.
[39] J.L. Mancuso, V. Van Speybroeck, The nature of extraframework aluminum species and Brønsted acid site interactions under catalytic operating conditions, J. Catal. 429 (2024) 115211, https://doi.org/10.1016/j.jcat.2023.115211.
[40] M. Ravi, V.L. Sushkevich, J.A. van Bokhoven, On the location of Lewis acidic aluminum in zeolite mordenite and the role of framework-associated aluminum in mediating the switch between Brønsted and Lewis acidity, Chem. Sci. 12 (2021) 4094–4103, https://doi.org/10.1039/D0SC06130A.
[41] G. Busca, Acid catalysts in industrial hydrocarbon chemistry, Chem. Rev. 107 (2007) 5366–5410, https://doi.org/10.1021/cr068042e.
[42] I. Lee, M.-S. Lee, L. Tao, T. Ikuno, R. Khare, A. Jentys, T. Huthwelker, C.N. Borca, A. Kalinko, O.Y. Gutiérrez, N. Govind, J.L. Fulton, J.Z. Hu, V.-A. Glezakou, R. Rousseau, M. Sanchez-Sanchez, J.A. Lercher, Activity of Cu–Al–Oxo extra-framework clusters for selective methane oxidation on Cu-exchanged zeolites, JACS Au 1 (2021) 1412–1421, https://doi.org/10.1021/jacsau.1c00196.
[43] J. Koppe, A.J. Pell, Structure determination and refinement of paramagnetic materials by solid-state NMR, ACS Phys. Chem. Au 3 (2023) 419–433, https://doi.org/10.1021/acsphyschemau.3c00019.
[44] A. Gervasini, S. Bennici, Dispersion and surface states of copper catalysts by temperature-programmed-reduction of oxidized surfaces (s-TPR), Appl. Catal. A. Gen. 281 (2005) 199–205, https://doi.org/10.1016/j.apcata.2004.11.030.
[45] R. Bulánek, B. Wichterlová, Z. Sobalík, J. Tichý, Reducibility and oxidation activity of Cu ions in zeolites, Appl. Catal. B 31 (2001) 13–25, https://doi.org/10.1016/S0926-3373(00)00268-X.
[46] J. Chen, W. Huang, S. Bao, W. Zhang, T. Liang, S. Zheng, L. Yi, L. Guo, X. Wu, A review on the characterization of metal active sites over Cu-based and Fe-based zeolites for NH_3 -SCR, RSC Adv. 12 (2022) 27746–27765, https://doi.org/10.1039/D2RA05107A.
[47] F. Gao, J. Szanyi, On the hydrothermal stability of Cu/SSZ-13 SCR catalysts, Appl. Catal. A. Gen. 560 (2018) 185–194, https://doi.org/10.1016/j.apcata.2018.04.040.
[48] J.D. Bjerregaard, J. Han, D. Creaser, L. Olsson, H. Grönbeck, Interpretation of H_2 -TPR from Cu-CHA using first-principles calculations, J. Phys. Chem. C 128 (2024) 4525–4534, https://doi.org/10.1021/acs.jpcc.3c07998.
[49] D. Nielsen, Q. Gao, T.V.W. Janssens, P.N.R. Vennestrøm, S. Mossin, Cu-speciation in dehydrated CHA zeolites studied by H_2 -TPR and In situ EPR, J. Phys. Chem. C 127 (2023) 12995–13004, https://doi.org/10.1021/acs.jpcc.3c01782.
[50] J. Song, Y. Wang, E.D. Walter, N.M. Washton, D. Mei, L. Kovarik, M.H. Engelhard, S. Prodinger, Y. Wang, C.H.F. Peden, F. Gao, Toward rational design of Cu/SSZ-13 selective catalytic reduction catalysts: implications from atomic-level understanding of hydrothermal stability, ACS Catal. 7 (2017) 8214–8227, https://doi.org/10.1021/acscatal.7b03020.
[51] X. Liu, X. Wu, D. Weng, Z. Si, R. Ran, Migration, reactivity, and sulfur tolerance of copper species in SAPO-34 zeolite toward NO_x reduction with ammonia, RSC Adv. 7 (2017) 37787–37796, https://doi.org/10.1039/C7RA06947B.
[52] S. Bordiga, E. Groppo, G. Agostini, J.A. van Bokhoven, C. Lamberti, Reactivity of surface species in heterogeneous catalysts probed by in situ X-ray absorption techniques, Chem. Rev. 113 (2013) 1736–1850, https://doi.org/10.1021/cr2000898.
[53] H. Praliaud, Surface and bulk properties of Cu–ZSM-5 and Cu/Al_2O_3 solids during redox treatments. Correlation with the selective reduction of nitric oxide by hydrocarbons, Appl. Catal. B 16 (1998) 359–374, https://doi.org/10.1016/S0926-3373(97)00093-3.
[54] F. Giordanino, P.N.R. Vennestrøm, L.F. Lundegaard, F.N. Stappen, S. Mossin, P. Beato, S. Bordiga, C. Lamberti, Characterization of Cu-exchanged SSZ-13: a comparative FTIR, UV-Vis, and EPR study with Cu-ZSM-5 and Cu-β with similar Si/Al and Cu/Al ratios, Dalton Trans. 42 (2013) 12741, https://doi.org/10.1039/c3dt50732g.
[55] A.S. Chikunov, S.A. Yashnik, O.P. Taran, A.Y. Kurenkova, V.N. Parmon, Cu(II) oxo/hydroxides stabilized by ZSM-5 zeolite as an efficient and robust catalyst for

chemical and photochemical water oxidation with Ru(bpy)33+, Catal. Today 375 (2021) 458–471, https://doi.org/10.1016/j.cattod.2020.07.009.
[56] C. Kalamaras, D. Palomas, R. Bos, A. Horton, M. Crimmin, K. Hellgardt, Selective oxidation of methane to methanol over Cu- and Fe-exchanged zeolites: the effect of Si/Al molar ratio, Catal. Lett. 146 (2016) 483–492, https://doi.org/10.1007/s10562-015-1664-7.
[57] C. Hammond, N. Dimitratos, R.L. Jenkins, J.A. Lopez-Sanchez, S.A. Kondrat, M. Hasbi ab Rahim, M.M. Forde, A. Thetford, S.H. Taylor, H. Hagen, E. E. Stangland, J.H. Kang, J.M. Moulijn, D.J. Willock, G.J. Hutchings, Elucidation and evolution of the active component within Cu/Fe/ZSM-5 for catalytic methane oxidation: from synthesis to catalysis, ACS Catal. 3 (2013) 689–699, https://doi.org/10.1021/cs3007999.
[58] X. Cui, H. Li, Y. Wang, Y. Hu, L. Hua, H. Li, X. Han, Q. Liu, F. Yang, L. He, X. Chen, Q. Li, J. Xiao, D. Deng, X. Bao, Room-temperature methane conversion by graphene-confined single iron atoms, Chem 4 (2018) 1902–1910, https://doi.org/10.1016/j.chempr.2018.05.006.
[59] W. Zhao, Y. Shi, Y. Jiang, X. Zhang, C. Long, P. An, Y. Zhu, S. Shao, Z. Yan, G. Li, Z. Tang, Fe-O clusters anchored on nodes of metal–organic frameworks for direct methane oxidation, angew. Chem. Int. Ed. 60 (2021) 5811–5815, https://doi.org/10.1002/anie.202013807.
[60] L.A. Gallego-Villada, E.A. Alarcón, F. Bustamante, A.L. Villa, One-pot tandem catalysis: green synthesis of β-pinene derivatives with MgO and mesoporous catalysts, J. Catal. 438 (2024) 115698, https://doi.org/10.1016/j.jcat.2024.115698.
[61] M.H. Groothaert, J.A. van Bokhoven, A.A. Battiston, B.M. Weckhuysen, R. A. Schoonheydt, Bis(μ-oxo)dicopper in Cu-ZSM-5 and its Role in the Decomposition of NO: a combined in Situ XAFS, UV−Vis−Near-IR, and Kinetic Study, J. Am. Chem. Soc. 125 (2003) 7629–7640, https://doi.org/10.1021/ja029684w.
[62] M.H. Groothaert, P.J. Smeets, B.F. Sels, P.A. Jacobs, R.A. Schoonheydt, Selective oxidation of methane by the bis(μ-oxo)dicopper core stabilized on ZSM-5 and mordenite zeolites, J. Am. Chem. Soc. 127 (2005) 1394–1395, https://doi.org/10.1021/ja047158u.
[63] P.J. Smeets, M.H. Groothaert, R.A. Schoonheydt, Cu based zeolites: a UV–vis study of the active site in the selective methane oxidation at low temperatures, Catal. Today 110 (2005) 303–309, https://doi.org/10.1016/j.cattod.2005.09.028.
[64] E. Borfecchia, K.A. Lomachenko, F. Giordanino, H. Falsig, P. Beato, A.V. Soldatov, S. Bordiga, C. Lamberti, Revisiting the nature of Cu sites in the activated Cu-SSZ-13 catalyst for SCR reaction, Chem. Sci. 6 (2015) 548–563, https://doi.org/10.1039/C4SC02907K.
[65] A.R. Kulkarni, Z.-J. Zhao, S. Siahrostami, J.K. Nørskov, F. Studt, Monocopper active site for partial methane oxidation in Cu-exchanged 8MR zeolites, ACS Catal. 6 (2016) 6531–6536, https://doi.org/10.1021/acscatal.6b01895.
[66] S. Sogukkanli, T. Moteki, M. Ogura, Selective methanol formation *via* CO-assisted direct partial oxidation of methane over copper-containing CHA-type zeolites prepared by one-pot synthesis, Green Chem. 23 (2021) 2148–2154, https://doi.org/10.1039/D0GC03645E.
[67] A.A. Gabrienko, A.A. Kolganov, S.A. Yashnik, V.V. Kriventsov, A.G. Stepanov, Methane to methanol transformation on Cu^{2+}/H-ZSM-5 Zeolite. characterization of copper state and mechanism of the reaction, Chem. –A Eur. J. 31 (2025), https://doi.org/10.1002/chem.202403167.
[68] J. Meyet, A. Ashuiev, G. Noh, M. Newton, D. Klose, K. Searles, A. van Bavel, A. Horton, G. Jeschke, J.A. van Bokhoven, C. Copéret, in: CH_4-to-CH_3OH on Mononuclear Cu(II) Sites Supported on Al_2O_3: Structure of Active Sites from Electron Paramagnetic Resonance, 2021, https://doi.org/10.26434/chemrxiv.13295879.v2.
[69] M.H. Ab Rahim, M.M. Forde, R.L. Jenkins, C. Hammond, Q. He, N. Dimitratos, J. A. Lopez-Sanchez, A.F. Carley, S.H. Taylor, D.J. Willock, D.M. Murphy, C.J. Kiely, G.J. Hutchings, Oxidation of methane to methanol with hydrogen peroxide using supported gold–palladium alloy nanoparticles, Angew. Chem. Int. Ed. 52 (2013) 1280–1284, https://doi.org/10.1002/anie.201207717.
[70] F. Ni, T. Richards, L.R. Smith, D.J. Morgan, T.E. Davies, R.J. Lewis, G.J. Hutchings, Selective oxidation of methane to methanol via in situ H_2O_2 synthesis, ACS Org. Inorg. Au 3 (2023) 177–183, https://doi.org/10.1021/acsorginorgau.3c00001.
[71] M.H. Mahyuddin, A. Staykov, Y. Shiota, K. Yoshizawa, Direct conversion of methane to methanol by metal-exchanged ZSM-5 zeolite (metal = Fe, Co, Ni, Cu, ACS Catal. 6 (2016) 8321–8331, https://doi.org/10.1021/acscatal.6b01721.
[72] Á. Szécsényi, G. Li, J. Gascon, E.A. Pidko, Mechanistic complexity of methane oxidation with H_2O_2 by single-site Fe/ZSM-5 catalyst, ACS Catal. 8 (2018) 7961–7972, https://doi.org/10.1021/acscatal.8b01672.